THE GEOLOGICAL SOCIETY OF AMERICA®

Clast arrangement influences fracture stratigraphy in a carbonate toe-of-slope megabreccia, Permian Rader Member, Bell Canyon Formation, Guadalupe Mountains, Texas, USA

Marat Ibagarov[1,†], Arnoud Slootman[1], Ted Playton[2], James Bishop[3], Vincent Heesakkers[3], Sergio Sarmiento[3], Piret Plink-Bjorklund[1], Lesli Wood[1], Rachel Aisner-Williams[1], and Zane R. Jobe[1]

[1]*Department of Geology and Geological Engineering, Colorado School of Mines, Golden, Colorado 80401, USA*

[2]*Matador Resources Company, Dallas, Texas 75240, USA*

[3]*Chevron Technical Center, a division of Chevron U.S.A. Inc., Houston, Texas 77002, USA*

ABSTRACT

Debris-dominated carbonate slopes comprise extensive volumes of margin-derived lithoclastic and skeletal components. While reefal margins and their steep slopes have been extensively studied and are actively targeted for hydrocarbon production, lower-angle distal slope settings remain less explored. Thus, there are limited insights into depositional processes, stratigraphic architecture, and fracture distribution within these settings, which all strongly influence fluid flow in the subsurface. To address these knowledge gaps, outcrop data were studied from the middle Rader Member megabreccia, a Permian carbonate toe-of-slope deposit exposed in Bell Canyon, Guadalupe Mountains, west Texas, USA. Multiscale sedimentological and structural observations, integrating drone-based digital outcrop models, photomosaics, scanlines, detailed graphic logs, and a novel square-meter grid-cell mapping method, were used to quantify internal architecture, clast-size distribution, matrix composition, and fracture patterns.

The studied outcrop, up to 25 m thick and exposed along ~700 m of depositional dip, exhibits repetitive lateral thinning caused by basal erosion and thickening due to the stacking of lithoclasts. Clast-size distributions show inverse grading of megaclasts (boulders exceeding 0.5 m) and normal grading of smaller clasts, along with repetitive downslope coarsening-to-fining patterns influenced by the presence of megaclasts. These observations suggest that the deposit at the studied locality was emplaced as a single event by a granular debris flow (i.e., a grain flow) with abundant particle collisions that promoted inverse grading of megaclasts.

Two fracture sets are present in the megabreccia, striking NE-SW and NW-SE, with broadly comparable dimensions and intensity. Fractures are rarely longer or taller than 0.5 m, with high aspect ratios, reflecting strong architectural confinement imposed by the inversely graded structure of the deposit. Larger and more dimensionally variable fractures occur preferentially in coarser, poorly sorted intervals, demonstrating textural control on fracture scaling. Preferential fracture propagation within the matrix of the megabreccia and frequent terminations at clast boundaries show that clasts act as mechanically competent inclusions, indicating that grain-to-matrix stiffness contrasts govern fracture growth. These findings show that extreme textural and mechanical heterogeneity fundamentally limits fracture growth, suggesting poor fracture-system connectivity in lower-slope carbonate megabreccias. The quantified relationships presented here aid the improvement of fracture-system prediction for reservoir models by incorporating the depositional processes and stratigraphic architecture that impact the resulting fracture geometries in carbonate megabreccia deposits.

INTRODUCTION

Among the end-member types of carbonate slopes (mud-, grain-, and debris-dominated systems; see Playton et al., 2010), debris-dominated slopes are particularly significant because they contain extensive margin-derived breccias in foreslope and toe-of-slope settings (Cook and Mullins, 1983; Mullins and Cook, 1986). These deposits record the recurrent growth and collapse of oligotrophic early-lithified boundstone factories, a persistent process that is common during slope development (e.g., Della Porta et al., 2003). Such systems typically form strike-extensive aprons dominated by breccia deposits, defined as clast-supported, gravel-rich sediment-gravity-flow deposits (McIlreath and James, 1978; Li et al., 2025). Breccias in these settings are internally composed of compensational, lens-shaped bodies that progressively backfill the slope (Playton and Kerans, 2018). At the toe-of-slope, these facies interfinger with grain-dominated or mud-dominated accumulations (Playton et al., 2010). Breccia deposits in all end-member slope settings are a target for hydrocarbon exploration (Karakitsios, 2013; Mazzuca et al., 2015; Amy, 2019), and many producing fields contain breccia deposits (e.g., Makassar Straits, Indonesia: Tanos et al., 2023; Permian basin, southwestern United States: Kvale et al., 2020; Poza Rica, Mexico: Janson et al., 2011; Tengiz, Kazakhstan:

Marat Ibagarov https://orcid.org/0009-0003-6200-8905
Arnoud Slootman https://orcid.org/0000-0001-8719-3041
Ted Playton https://orcid.org/0000-0002-5761-5511
James Bishop https://orcid.org/0009-0009-7041-8959
Vincent Heesakkers https://orcid.org/0000-0002-2549-3732
Sergio Sarmiento https://orcid.org/0009-0006-8672-1192
Piret Plink-Bjorklund https://orcid.org/0000-0003-1637-2100
Lesli Wood https://orcid.org/0000-0002-7011-0905
Rachel Aisner-Williams https://orcid.org/0000-0002-4595-1948
Zane R. Jobe https://orcid.org/0000-0002-7654-4528
[†]mibagarov@mines.edu

GSA Bulletin; https://doi.org/10.1130/B39263.1.

For permission to copy, contact editing@geosociety.org
© 2026 Geological Society of America

Collins et al., 2014; Karachaganak, Kazakhstan: Katz et al., 2010).

While there has been significant focus on the sequence stratigraphic framework and initiation mechanisms of breccia deposits (e.g., Spence and Tucker, 1997; Playton and Kerans, 2018), their depositional-process framework has received less attention (e.g., Drzewiecki and Simó, 2002; Li et al., 2025). Depositional processes determine the texture, bed thickness, clast size, and vertical stacking patterns in toe-of-slope breccia deposits, which in turn control the mechanical properties and burial-fracture distribution (Shackleton et al., 2005; Laubach et al., 2019). The resulting "fracture stratigraphy" (Laubach et al., 2009) is important for characterizing subsurface reservoir fracture connectivity, yet most mechanical stratigraphy studies to date have concentrated on carbonate platform tops and margins (e.g., Cooke et al., 2006; Wennberg et al., 2007; Barbier et al., 2012). Fracture characterization of breccia reservoirs based solely on well data remains challenging because heterogeneous clast fabrics, short mechanically constrained fractures, and commonly steep dips can obscure or mimic fracture signatures in logs, systematically underestimating fracture abundance and connectivity (Playton et al., 2025a). Thus, outcrop-based analysis that links the depositional processes and spatial changes in depositional fabric to the variability in fracture distribution is essential for constraining uncertainties in reservoir behavior and improving development and production strategies (e.g., Narr et al., 2024).

This study focused on the middle Rader submember (Lawson, 1989) of the Bell Canyon Formation (King, 1948), here referred to as the middle Rader megabreccia, an outer-shelf-, reef-, and slope-derived carbonate toe-of-slope breccia exposed in the Guadalupe Mountains of west Texas, USA. Although previous work on the Rader Member and the middle Rader megabreccia documented its stratigraphic position (King, 1948) and facies characteristics (e.g., Lawson, 1989; Playton et al., 2025b), quantitative characterization of clast-size distributions and fracture dimensions has not been undertaken. To address these gaps, we integrated multiscale sedimentological and structural observations, including drone-based digital outcrop models, photomosaics, scanlines, detailed graphic logs, and a novel square-meter grid-cell mapping method. These integrated observations enabled us to evaluate the influence of breccia architecture and clast organization on fracture initiation, propagation, and spatial distribution, thereby establishing the foundation for improved prediction of fracture behavior in carbonate breccia reservoirs.

Geologic Setting

The initiation of the Permian Basin, one of the most prolific hydrocarbon basins in the world (Ruppel, 2019), is linked to the late Carboniferous Ouachita-Marathon orogeny that reactivated deep-rooted Precambrian structures (Yang and Dorobek, 1995). The resulting bounding and intraforeland uplifts subdivided the basin, with the Central Basin Platform dividing the western Delaware Basin and eastern Midland Basin. The carbonate margin architecture that fringed these basins evolved from a distally steepened ramp to a reef-rimmed margin over a period of 11 m.y. during the middle Permian in an arid, subequatorial setting (Kerans et al., 2014, 2021). The Guadalupe Mountains (Fig. 1) expose this shelf-to-basin depositional profile located in the northwestern portion of the Delaware Basin (Fig. 1C). The youngest, Guadalupian-aged Capitan system spans ~5 m.y. and includes three composite sequences (Fig. 2) that contain platform-top

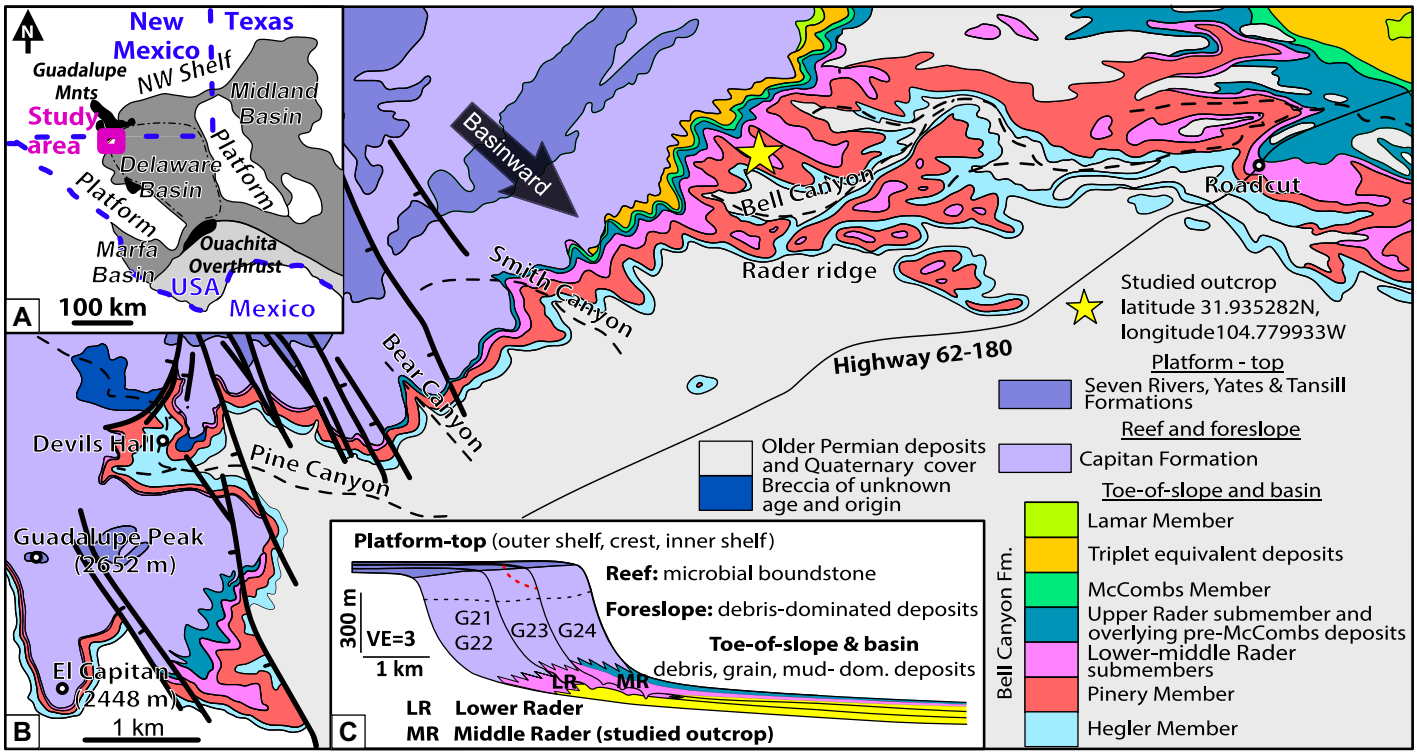


Figure 1. (A) Early Permian paleogeographic map of the Permian Basin, modified from Playton and Kerans (2018). (B) Geologic map of the Guadalupe Mountains, modified from Playton et al. (2025b) after original map from King (1948). Rader Member terminology is from Lawson (1989). (C) Simplified sequence architecture along the Delaware Basin northwest shelf showing high-frequency sequences, simplified from Playton et al. (2025b). VE—vertical exaggeration. Sequence framework (G22–G24) is after Tinker (1998), Kerans and Tinker (1999), Kerans and Kempter (2002), Playton (2008), Kerans et al. (2012, 2014, 2021), Playton and Kerans (2018), and Playton et al. (2025b).

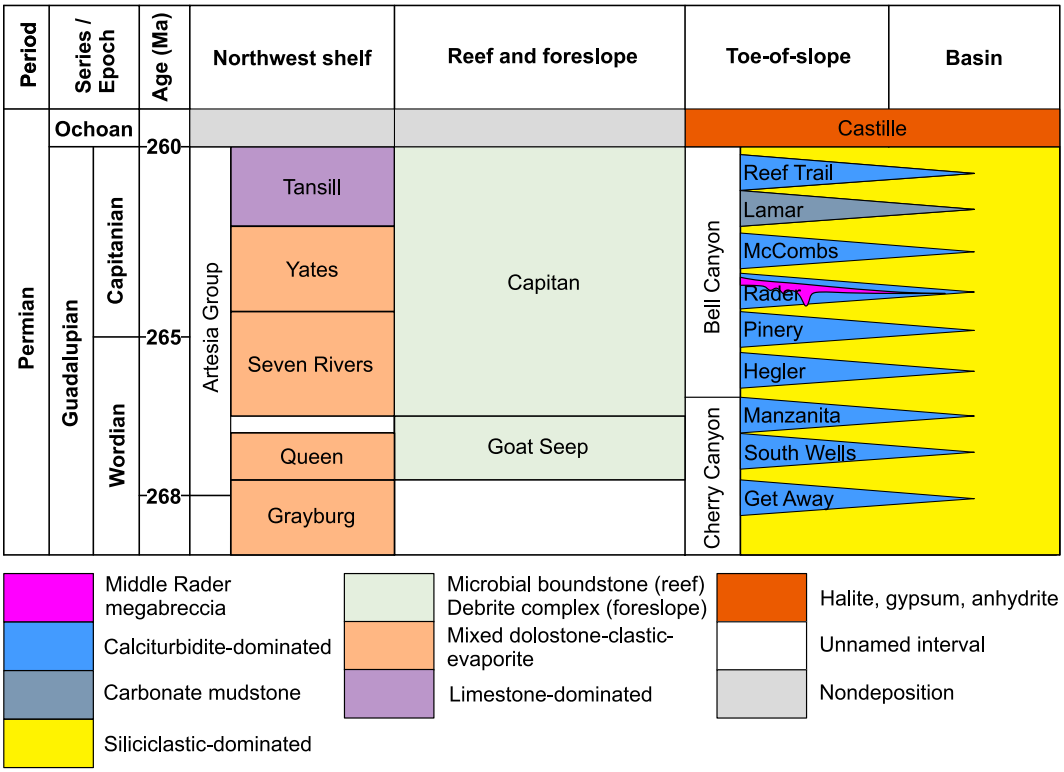


Figure 2. Stratigraphic chart of the Guadalupian section, showing the correlation from the Guadalupe Mountains to the Delaware Basin (after Kerans et al., 2014, 2021). The middle Rader megabreccia is contained within the Rader Member. Stratigraphy is simplified from Ruppel (2019). Original subdivisions and stratigraphic relationships are from King (1948).

(Seven Rivers, Yates, and Tansill Formations) to reef and associated foreslope (Capitan Formation) and toe-of-slope deposits (Bell Canyon Formation) (King, 1948; Tinker, 1998; for an extensive review, see Playton and Kerans, 2018). Within this overall progradational succession, 14 high-frequency sequences (HFS G17–G30) are identified (Tinker, 1998; Kerans et al., 2014).

Rader Member of the Bell Canyon Formation

The Bell Canyon Formation represents the toe-of-slope and basinal deposits time-equivalent to the Capitan system. The formation is composed of carbonate-rich members (King, 1948) that intercalate with, and transition into, basinal siliciclastics: the Hegler, Pinery, Rader, McCombs, and Lamar Members (Figs. 1 and 2). The Rader Member is subdivided into three submembers (Lawson, 1989) that correspond to HFS G21–G24 (Playton et al., 2025b). The Lower Rader submember is a grain-dominated unit and comprises HFS G21–G22, recording highstand systems tract (HST) deposition. The middle Rader submember is a breccia-dominated unit and contains the lower portion of G23, representing lowstand systems tract (LST) conditions and a period of margin instability (Playton et al., 2025b). The Upper Rader submember is a grain-dominated unit and represents the HST of G23 and the transgressive systems tract (TST) of G24 (Playton et al., 2025b). All three submembers contain interbedded lowstand siliciclastic sediments that vary spatially along strike and increase in proportion distally (King, 1948; Lawson, 1989; Playton et al., 2025b).

The most detailed study of the middle Rader megabreccia was carried out by Lawson (1989), who mapped the facies architecture to determine the source of the breccia and associated depositional processes. With the available outcrop extent, Lawson (1989) was able to trace the deposit for at least 17 km downdip from the Guadalupe Mountains front, and for a minimum of 10 km along strike before it dips into the subsurface. Architecturally, the proximal middle Rader megabreccia is characterized by channelized geometries, coarser clasts, and clast-supported fabric, typified by outcrops along Rader Ridge (Fig. 1). Toward distal settings, the siliciclastic matrix percentage increases and clast size decreases, with some outsized clasts present; these distal facies are well exposed at the "Rader road cut" along U.S. Highway 62/180 ~5 km southeast of the coeval shelf margin (Lawson, 1989; Playton et al., 2025b). Lawson (1989) identified the most common clast compositions as skeletal-peloidal wackestones to grainstones, floatstone to rudstone with a wacke-grainstone matrix (i.e., clasts of earlier generation), and reef-derived boundstone, suggesting that the megabreccia was sourced predominantly from the outer shelf, reef, and foreslope, with no evidence of contributions from the shelf crest or inner-shelf settings.

Most authors (e.g., Newell et al., 1953; Rigby, 1958; Lawson, 1989; Playton et al., 2025b) agree that the middle Rader megabreccia is not a single mass failure, but rather a protracted time interval of mass wasting of the margin that sculpted the seafloor through sediment-gravity-flow erosion and deposition. In contrast, Hornbuckle (2017) and Moreland (2018) modeled the sediment volume of the middle Rader megabreccia as a potential single-collapse source for tsunami generation. Even though the middle Rader megabreccia is an important outcrop analog for many breccia-dominated slope systems (sensu Playton et al., 2010), its detailed depositional-process framework remains poorly constrained.

Fracture and Fault Development in the Bell Canyon Formation

The formation, subsidence history, and subsequent deformation of the Permian Basin were complex and multiphase (for a more complete review, see Hill, 1996; Ruppel, 2019; Fairhurst et al., 2021). Deposition of the Bell Canyon Formation was not affected by active tectonism, but rapid progradation of the Capitan margin caused gravitational loading and differential compaction of slope and basin deposits that resulted in syn-sedimentary faults and fractures in outer-shelf and reef deposits that strike margin-parallel (~030°) and margin-perpendicular (~140°) (Hunt et al., 2003; Koša and Hunt, 2005; Rush and Kerans, 2010; see also mapped clinoforms

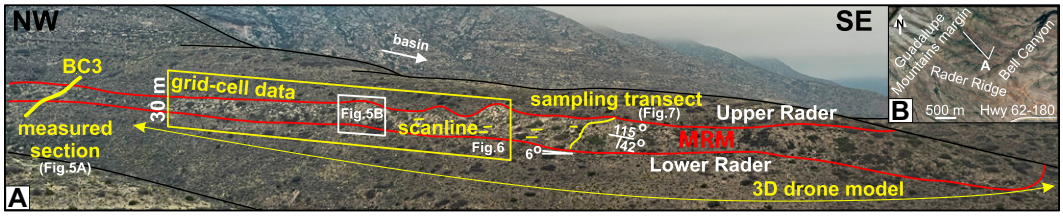


Figure 3. (A) Oblique-dip view of the studied middle Rader megabreccia (MRM) outcrop exposed along the northeast wall of Bell Canyon showing locations and types of field data collected. (B) Location map of the studied outcrop. See also Figure 1 for the location.

of Playton and Kerans, 2018). During burial of the Bell Canyon Formation, burial fractures may have developed, but no study has yet dated veins to unequivocally demonstrate the timing and age constraints for deducing burial versus tectonic fracture timing. The period of relative tectonic quiescence was later disrupted by eastward-directed compression during the Laramide orogeny (80–55 Ma) that caused regional uplift, slight tilting to the east, and the development of tectonic (i.e., vertical) stylolites striking NNE-SSW (Hill, 1996). These stylolites have not been observed in the middle Rader megabreccia within our study area. A progressive change in stress from Laramide compression to Basin-and-Range extension was completed by the late Oligocene (30 Ma), causing ENE-oriented tensional stress that resulted in high-angle normal faulting and, according to some authors, continued uplift (for discussion, see Hill, 1996). Basin-and-Range extension had arguably the most profound effect on the fracture and joint networks in the Bell Canyon Formation, which are parallel to NNW-SSE–trending fault systems that form the prominent Western and Algerita Escarpments (King, 1948; Hill, 1996; Koša and Hunt, 2006). Extensional deformation continued at least into the late Quaternary (Machette and Jochems, 2015), contributing to the excellent exposure and topographic steepness of the Guadalupe Mountains. Collectively, fractures in carbonate slope deposits are multigenerational, including syndepositional fractures that are tall, irregular, and filled with marine sediment and radiaxial-fibrous calcite; deeper burial fractures that are small, planar, and filled with blocky calcite; and late uplift-related joints that are planar, sparsely mineralized or barren, and locally enlarged by meteoric dissolution (Narr et al., 2024). Syndepositional fractures are abundant in reef and upper-slope settings, whereas burial fractures may occur throughout slope deposits, following lithification and burial of the host strata to depths of 1–1.5 km (Kerans, 1985; Wallace et al., 1991).

DATA COLLECTION METHODOLOGY

The studied outcrop is exposed on the northeastern wall of Bell Canyon in the Guadalupe Mountains, west Texas (Fig. 3) and represents an oblique-dip section (outcrop strike is 115°, regional depositional dip direction is 140°; Figs. 1 and 3). The field dataset incorporated both sedimentological and structural observations to characterize the fracture stratigraphy of the middle Rader megabreccia. A georeferenced digital outcrop model ~800 m long × 50 m high was created using photos from a DJI Mavic 3 Pro quadcopter and Agisoft Metashape software. From this model, a 300 × 30 m georeferenced orthomosaic oriented perpendicular to the outcrop face was generated and used in the field to document stratal geometries, facies architecture, graphic logs, clast size, sample collection for X-ray fluorescence (XRF) analysis, and fracture characterization (Fig. 3).

A novel square-meter grid-cell mapping technique was used, in which the orthomosaic was overlaid with 1 m^2 cells in QGIS, and each grid cell was systematically visited to document sedimentological and fracture data (see the following section for details). Outcrop weathering and vegetation limited the number of cells that could be documented to 2441 out of 4445 cells in total (i.e., 55% of the cells had sufficient exposure for data collection). Although weathered and vegetated areas accounted for the undocumented cells, these areas were spatially patchy and typically coincided with megaclasts (covering 1584 cells), locally exposing 10 × 10 m continuous outcrops that enabled us to document the conceptual sedimentary texture of the middle Rader megabreccia. This workflow enabled spatially consistent, high-resolution quantification of clast-size distribution, matrix proportion, and fracture attributes, allowing direct comparison of their spatial trends within this complex breccia outcrop.

Sedimentological Data

Sedimentological data collected in each square-meter cell included clast size, matrix texture (i.e., clast- vs. matrix-supported), matrix-to-clast ratio, and matrix composition (carbonate-dominated or siliciclastic-dominated). Clast size is expressed in psi (ψ) units (inverse of phi), where $\psi = \log_2(D)$, with D being the clast maximum apparent diameter in millimeters (Fig. 4; for terminology, see Blott and Pye, 2012), and reported in descriptive statistics, namely, D_{50} (median clast size; 50th percentile by area) and D_{90} (coarse fraction; 90th percentile by area). Lithoclasts >0.5 m in maximum apparent diameter are termed megaclasts and were mapped individually and were also incorporated into the D_{50} and D_{90} clast-size estimation of grid cells. For megaclasts, maximum and minimum apparent diameters were measured to constrain aspect ratios (Fig. 4).

Lithoclasts are distinguished in the field by their pale-gray color and relatively homogeneous weathering, contrasting with the surrounding light-brown to yellow matrix. This color contrast facilitates consistent and minimally biased megaclast mapping and size estimation. However, it can locally be problematic because the same allochems often appear within both lithoclasts and matrix. For instance, loose carbonate allochems >2 mm (e.g., fusulinids) are present in the matrix fraction of the middle Rader megabreccia (Lawson, 1989) and in age-equivalent foreslope breccias (Playton and Kerans, 2018). Consequently, we prefer a 3 mm grain-size cutoff between matrix and clasts, although a 2 mm allochem size cutoff is widely accepted to define grainstone from rudstone/floatstone (Dunham, 1962; Lokier and Al-Junaibi, 2016). On this basis, matrix samples were collected at 1 m intervals along a transect (Fig. 3) and subsequently analyzed using portable X-ray fluorescence (pXRF; Bruker TRACER-5 with helium flow) at Colorado School of Mines and by X-ray diffraction (XRD) at RohmTek, Houston, Texas.

In addition to the grid-cell data collection method described above, the measured section further characterizes the sedimentology of the Rader Member. The graphic log (Fig. 3) utilized classifications for grain size and carbonate texture from both Wentworth (1922) and Dunham (1962), respectively, modified by Embry and Klovan (1971). These logs were digitized using the methods of Jobe et al. (2021) in EasyCore software to enable quantification of grain size and bed thickness.

Fracture Data

Fracture data ($n = 1514$) were collected using four complementary methods (Table 1): (1)

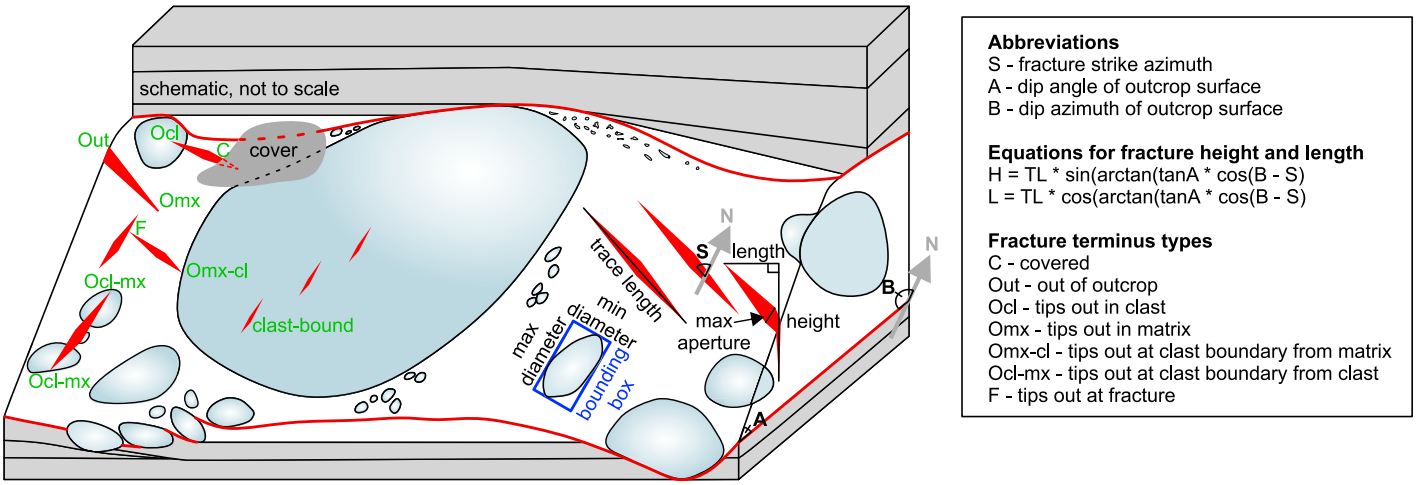


Figure 4. Schematic illustration for fracture parameters measured in the middle Rader megabreccia. Fracture termini are indicated in green. Maximum apparent diameter of clasts is the long edge of the best-fitting bounding box, indicated in blue. Fracture height (H) and length (L) were calculated using fracture trace length (TL) and outcrop surface orientation (dip and azimuth).

TABLE 1. SUMMARY OF FRACTURE DATA (N = 1514) COLLECTED FROM THE MIDDLE RADER MEGABRECCIA (BELL CANYON, GUADALUPE MOUNTAINS, WEST TEXAS, USA) USING FOUR COMPLEMENTARY METHODS

Method 1: Scan-line dataset (mineralized fractures)			
Total coverage, *n* and total length of scan lines			*n* = 6, totaling 23.12 m
Fractures measured			*n* = 143
Strike azimuth			*n* = 143
Dip angle			*n* = 122, median = 85°
Height			*n* = 136, median = 0.1 m
Length			*n* = 143, median = 0.2 m
Maximum aperture			*n* = 134, median = 0.25 mm
Terminus (upper, lower, side 1, side 2)			*n* = 449
Method 2: Digital outcrop model dataset (mineralized fractures and open joints)			
Total coverage			~250,000 m^3
Fractures measured			*n* = 297
Strike azimuth and dip angle			Median dip angle = 79°
Height and length			Median height = 0.5 m Median length = 0.11 m
Method 3: Targeted fractures dataset (mineralized fractures and megaclast dimensions)			
3A	Longest fractures present in the exposure	Fractures measured	*n* = 152
		Strike azimuth	*n* = 152
		Dip angle	*n* = 79, median = 82°
		Trace length	*n* = 152, median = 0.49 m
		Maximum aperture	*n* = 145, median = 0.4 mm
		Terminus	*n* = 278
3B	Clast-bound fractures	Fractures measured	*n* = 87
		Strike azimuth	*n* = 87
		Trace length	*n* = 87, median = 0.22 m
		Maximum aperture	*n* = 87, median = 0.30 mm
		Terminus	*n* = 174
		Clasts max and min diameters, surface orientation	*n* = 31 Median maximum apparent diameter = 0.82 m Median minimum apparent diameter = 0.39 m
Method 4: Grid-cell dataset (mineralized fractures and clast size, i.e., D_{50}, D_{90}, and megaclast dimensions)*			
Total coverage (covered and noncovered exposures)			4445 grid cells (1 m^2 each)
Data collected from area (noncovered exposure)			2441 grid cells (1 m^2 each)
Fractures measured (trace length, strike, terminus, maximum aperture)			*n* = 835, measured from 741 grid cells Median trace length = 0.2 m Median max. aperture = 0.4 mm
D_{50}, D_{90}, roundness, matrix vs. clast percentage			*n* = 857 grid cells Median D_{50} = 0.17 m Median D_{90} = 0.44 m
Megaclasts (boulders >0.5 m in maximum apparent diameter)			*n* = 658, occupying 1584 grid cells Median maximum apparent diameter = 3.4 m Median minimum apparent diameter = 2.0 m

*D—maximum apparent clast diameter; D_{50}—median clast size, 50th percentile by area; D_{90}—coarse fraction, 90th percentile by area.

along scanlines in the field, (2) from the digital outcrop model, (3) from targeted fractures in the field, and (4) using the grid-cell method; each of these methods is described below. These approaches were selected to capture different aspects of fracture characteristics and distribution across multiple scales. Only fractures with a minimum trace length of 5 cm were measured in all methods; however, these measurements represent minimum apparent dimensions because each exposed trace corresponds to an unknown intersection through a 3-D fracture surface. (1) Six bedding-parallel scanlines were collected (cf. Ortega et al., 2010) to provide systematic and relatively unbiased estimates of mineralized fracture orientation, termination types, spacing, intensity (calculated using method of Terzaghi, 1965), and dimensions (Table 1). (2) Fractures from the digital outcrop model were interpreted using the polyline tool in Virtual Reality Geological Studio software (Hodgetts et al., 2015; Table 1), enabling remote characterization of most extensive fractures and joints, particularly their orientation (azimuth and dip angle) and dimensions (length and height). (3) Targeted fractures were collected to document the upper tail of the mineralized fracture size distribution, including (3A) large and (3B) clast-bound fractures (Table 1).

The grid-cell fracture dataset (item 4 in the previous paragraph) comprises the majority of measurements (n = 835; Table 1) and includes fracture azimuth, trace length, maximum aperture, and terminus type (in addition to the sedimentological data described in the previous paragraph). For each cell, the longest mineralized fracture was selected for measurement, and occasionally a second fracture was measured if

its trace length also exceeded 5 cm. Fractures extending across multiple grid cells were documented only once and assigned to the cell where their maximum aperture was observed. Measuring all fractures within each cell is impractical, as it would considerably increase sampling effort without substantially improving characterization of the largest fractures, the most influential fractures for reservoir connectivity, geomechanical behavior, and reservoir modeling. As such, interpretations based on the grid-cell dataset focused on spatial variability in the largest mineralized fracture dimensions rather than fracture density or the full distribution of fracture dimensions within each cell.

For (3) targeted and (4) grid-cell methods, fracture height and length could often not be measured directly due to the rounded nature of the outcrop exposure and small size of the fractures. Instead, trace length was measured (i.e., the fracture length along an exposure surface), which was then trigonometrically converted to fracture height and length using the average orientation of the outcrop (115° strike and 42° dip angle toward 205° azimuth; see Fig. 5). We acknowledge that this approach assumes a representative outcrop orientation, and local variability in exposure geometry introduces uncertainty into fracture height and length estimates. To evaluate this uncertainty, we tested the conversion using several outcrop dip angles (42°, 32°, and 17°) and compared the resulting height and length distributions to those obtained from scan-line measurements, where fracture height and length were directly measured. The dip angle of 42° yielded distributions most similar to fracture dimensions measured from scanlines (Table 1), lending confidence to the trace-length to height or length calculations. In addition, given that measured trace lengths were generally small (rarely exceeding 0.5 m; Table 1), the magnitude of potential error in outcrop orientation is limited.

Maximum aperture and terminus type of fractures were documented directly for all methods

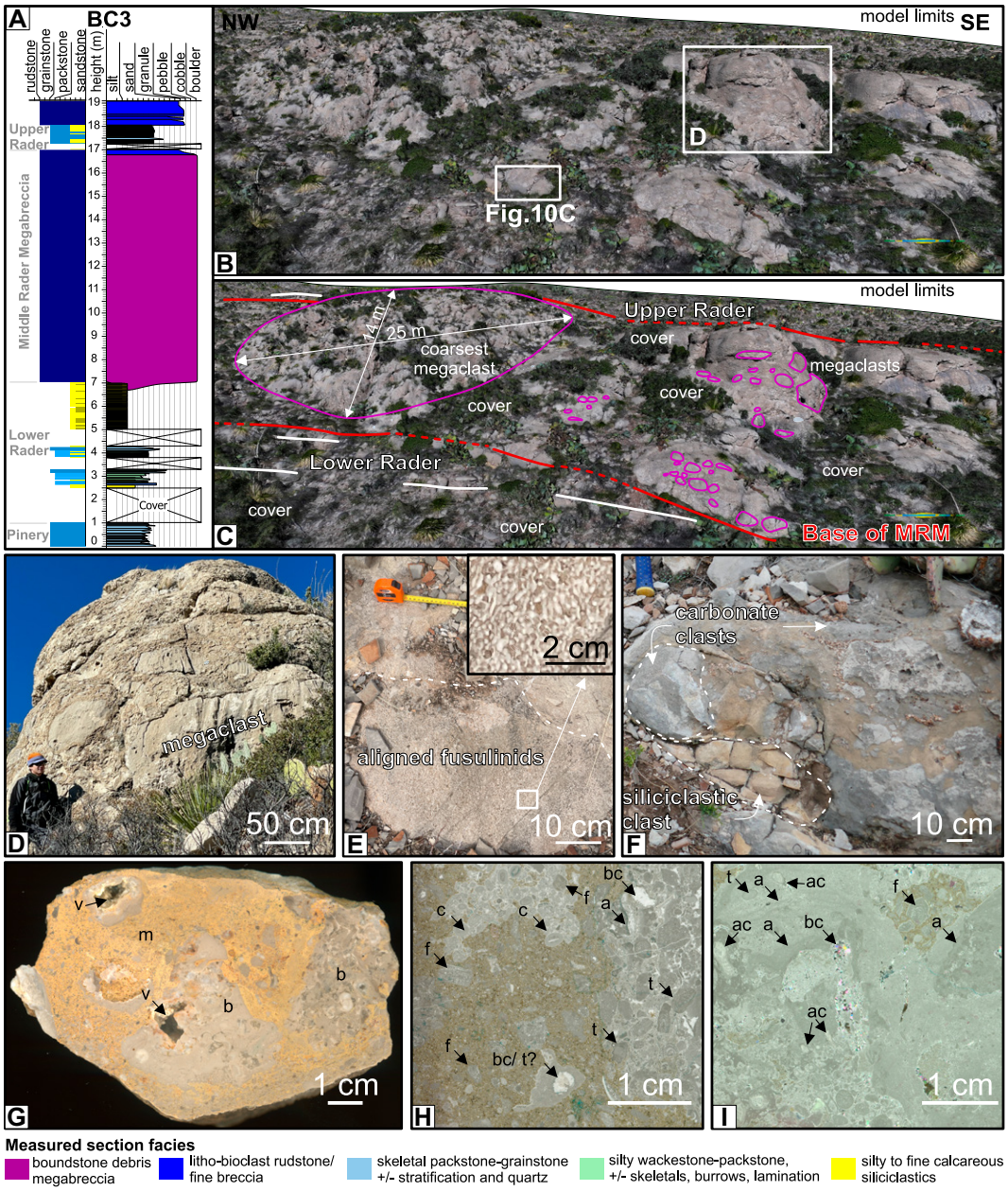


Figure 5. (A) Graphical log of the measured section BC3. Lithofacies are from Playton and Kerans (2018). See Figure 3 for location. (B) Uninterpreted and (C) interpreted view of the middle Rader megabreccia (MRM) from the 3-D digital outcrop model (see Fig. 3 for location). The lower-middle Rader megabreccia contact is erosional, and the upper contact has positive topography related to megaclasts. Note the textural differences between matrix and outlined megaclasts. White rectangle shows close-up location of part D. (D) Typical exposure of the middle Rader megabreccia, with visible megaclasts. (E) Outlined lithoclast composed of aligned fusulinids (see inset). (F) Lithoclasts are predominantly of carbonate composition, but minor siliciclastic (laminated sandstone) lithoclasts are present. (G) Polished slab showing boundstone lithoclasts (b) in a siliciclastic matrix (m) composed of silt to fine quartz sand mixed with carbonate skeletal grains. Note the vugs (v) in the boundstone that are partially filled with calcite cement. (H, I) Thin sections showing lithoclasts and surrounding matrix. Allochems include botryoidal marine cement (bc), fusulinids (f), *Acanthocladia* (ac), *Tubiphytes* (t), and *Archaeolithoporella* (a). Coated grains (c) are also present.

except for the digital outcrop model (item 2 in this section) due to inadequate resolution. Seven terminus types were identified (Fig. 4): termination in a clast (Ocl), in the matrix (Omx), at another fracture (F), at a clast–matrix boundary from the clast to the matrix (Ocl-mx) or from the matrix to the clast (Omx-cl), not exposed (Out) and covered (C). Fractures terminating at both ends within a single clast were classified as clast-bound fractures.

RESULTS

Sedimentology

Sections measured by Lawson (1989), Playton et al. (2025b), and this study (Fig. 5A) recognize three Rader Member submembers: The Lower Rader and Upper Rader submembers are composed of graded packstone to grainstone calciturbidites that are occasionally interbedded with silt-to-sandstone turbidites, while the Middle Rader submember (i.e., middle Rader megabreccia) is composed of clast-supported breccia with a mixed siliciclastic and carbonate matrix. In outcrop, lithoclasts appear pale gray in color and contrast with the light-brown matrix, making clast boundaries visually distinct (Figs. 5B–5D). Megaclasts stand out by their size (>0.5 m), subrounded shape (Figs. 5B–5D), and homogeneous weathering, commonly displaying an etched and pitted surface due to partial dissolution by rainwater, resulting in a rough, fretted texture with sharp-edged protrusions. Compositionally, reef-derived lithoclasts are common, featuring *Tubiphytes* colonies and *Acanthocladia* encrusted by *Archaeolithoporella* (Fig. 5I). Lithoclasts derived from outer-shelf facies are also present, including aligned *Polydiexodina*-bearing fusulinid packstone (Fig. 5F), skeletal packstone with large benthic *Polydiexodina*, and grainstone with grains encrusted by *Tubiphytes* (Figs. 5G and 5H). Although carbonate clasts dominate, rare but well-preserved rip-up clasts of laminated toe-of-slope sandstone and siltstone occur near the base of the deposit (Fig. 5E). In the distal extent of the studied outcrop (Fig. 3), the middle Rader megabreccia appears more homogeneous, and clast boundaries are less obvious (cf. Lawson, 1989); these areas, while not the focus of this study, can be interpreted either as a carbonate-matrix–rich breccia with indistinct clast boundaries or as a complex of large boulders with minor matrix.

The thickness of the megabreccia ranges from 11 m to 24 m with an average of ~15 m. The thickness variability reflects an incised erosional base and localized topographic highs on the top, associated with the occurrence of megaclasts (Figs. 6A–6B). The most pronounced thickness change occurs at ~250 m distance in the orthomosaic panel, where the megabreccia rapidly thickens from 11 m to 23 m over a lateral distance of ~24 m. This thickening corresponds to a 7-m-deep basal scour, and a 5-m-thick bulge at the top caused by the presence of an exceptionally large megaclast. The internal architecture of the middle Rader megabreccia is complicated by spatial trends in clast-size distribution (Figs. 6C–6D), sorting (Fig. 6E), and matrix content (Fig. 6F), which are described in detail later in this section. However, internal surfaces, vertical grading units, or matrix changes that would indicate distinct event beds within the megabreccia within our detailed, 300-m-long

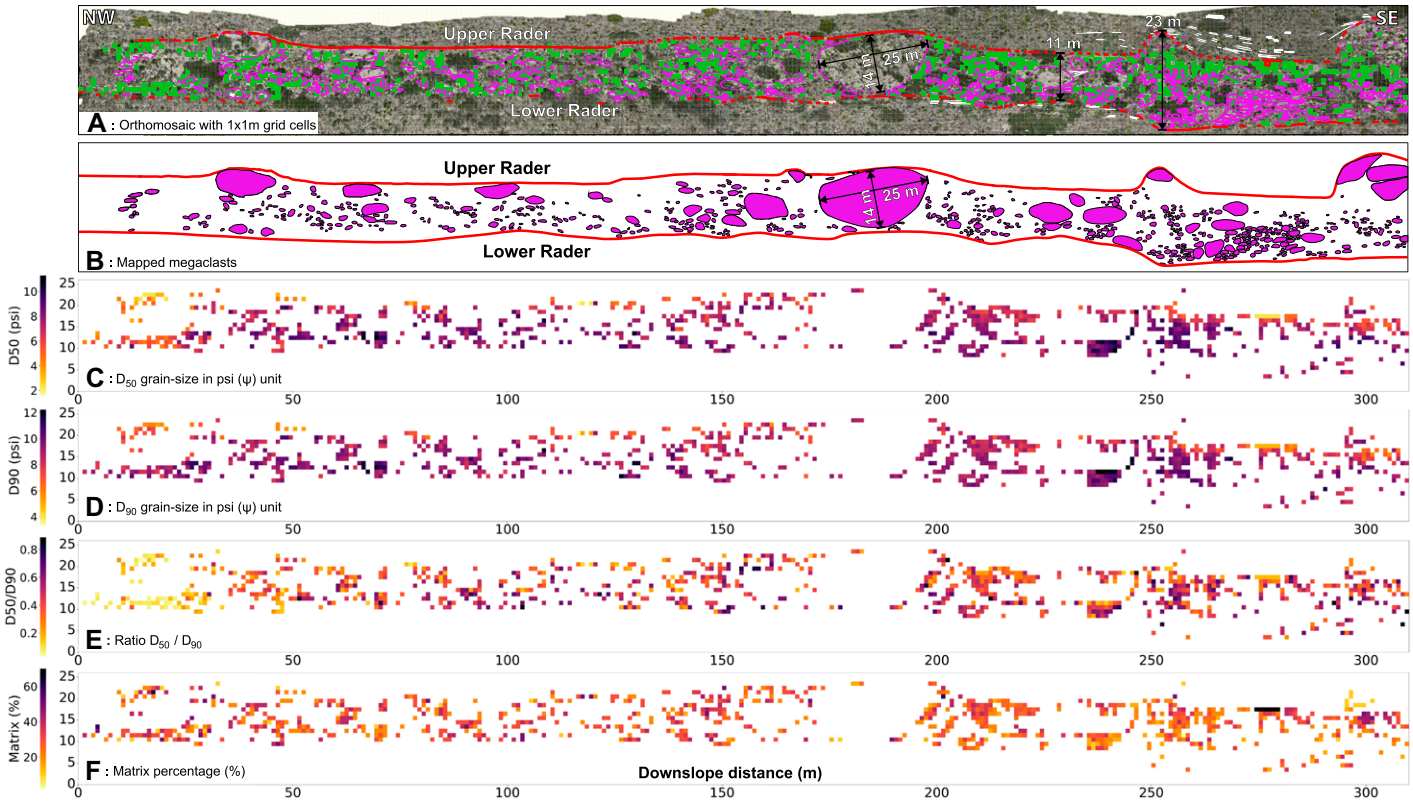


Figure 6. (A) Orthomosaic image overlaid with the square-meter grid cells and a coordinate system used to map megaclasts (pink polygons) and locate individual cells (green squares) in the field for documenting clast-size distribution (D_{50} and D_{90}), matrix content, and fracture dimensions. (B) Simplified view showing the middle Rader megabreccia boundaries and mapped megaclasts. (C–F) Sedimentological parameters are displayed separately in heatmaps, showing distributions of (C) D_{50}, (D) D_{90}, (E) ratio of D_{50} to D_{90}, and (F) matrix proportion across cells.

grid window were not observed. Also, no consistent relationship between exposure thickness and matrix content was identified.

Vertical Transect Data

A vertical transect measured across the middle Rader megabreccia revealed systematic variations in both clast size and geochemical composition (Fig. 7). Clast-size data show considerable variability but display an overall fining-upward trend (Fig. 7B). Maximum apparent diameters (D_{max}) range from coarse gravel to fine pebble sizes (1–10 ψ), whereas minimum apparent diameters (D_{min}) are generally finer (3–8 ψ). The 5–11 m vertical interval contains the largest clasts, while the uppermost 3 m are characterized by distinctly finer and better-sorted clasts. XRF characterization (Fig. 7C) shows that calcium (Ca) comprises ~30% of the matrix, whereas silicon (Si) remains consistently low (1–3 wt%) throughout the section. Although the matrix appears siliciclastic in outcrop (Fig. 5E) and was described as such by Lawson (1989), XRF data indicate that it is carbonate-dominated, with only minor dispersed siliciclastic components. Notably, magnesium (Mg) shows pronounced variability along the sampling transect, with concentrations increasing from ~0.1 wt% to nearly 10 wt% within the middle (6–11 m) and uppermost (13–16 m) intervals, indicating localized dolomitization of the matrix that coincides with finer-clast texture. Detrital elements such as aluminum (Al), silicon (Si), potassium (K), titanium (Ti), and iron (Fe) show higher concentrations in the lower part of the transect. One XRD measurement from the 5–6 m interval confirms the XRF data, with 91.2% calcite, 5.7% quartz, 0.5% K-feldspar, 2% clay, and 0.2% other.

Grid-Cell Sedimentological Data

In the spatial clast-size distribution, across all grid-cells, D_{50} values range from 0.3 cm (1.7 ψ) to 2.5 m (11.3 ψ), with a median of 17 cm (7.4 ψ; Fig. 8A), while D_{90} values vary from 1 cm (3.3 ψ) to 6.0 m (12.6 ψ), with a median of 44 cm (8.8 ψ), approximately twice the median D_{50}. Megaclasts are slightly elongated with a median aspect ratio of 1.8 (long axis/short axis), with their long axis generally oriented in a sub-horizontal position (Figs. 5B and 6A). Megaclast maximum apparent diameters range from 0.5 m to 25 m (9.0–14.6 ψ), with a median of 3.4 m (11.7 ψ), while the minimum apparent diameters range from 0.13 m to 14 m (6.6–13.8 ψ), with a median of 2.0 m (11.0 ψ; Fig. 8A).

The vertical clast-size distribution (Fig. 8B) in the megabreccia was created by grouping data by vertical position of cells (Fig. 6A) normalized to the local deposit thickness (i.e., normalized thickness). Clast-size distributions <0.5 m in diameter (i.e., non-megaclasts) exhibit an overall normal grading as shown by the kernel density estimations (KDEs) of D_{50} and D_{90}, with a weakly inversely graded layer in the lower third of the deposit (Fig. 8B). In contrast, the KDEs for megaclast-size distribution (>0.5 m) show an inverse grading trend, with the largest clasts "floating" at the top of the megabreccia (Fig. 8B).

Downslope trends in D_{50} and D_{90} are variable along the measured 300 m window of exposure (Fig. 9). In the proximal part of the window, several repetitive downslope-coarsening intervals were observed (Fig. 9B), each linked to the emplacement of megaclasts, including the largest measured boulder (25 × 14 m; Fig. 9A), which accounts for the entire thickness of the megabreccia at ~160 m downslope position. Immediately downslope of this megaclast (175–220 m), D_{50} and D_{90} of the lithoclasts show a narrow range in values with a downslope-fining trend over a span of ~50 m (Fig. 9), where megaclasts are smaller and better sorted. This repetitive coarsening trend is disrupted between 220 m and 300 m by the reappearance of coarser megaclasts, which coincide with a general greater variability in both D_{50} and D_{90} in this area.

The coarsening trends coincide with thickness increases of the megabreccia, where megaclasts at the distal end of the intervals generate topographic highs that locally thicken the deposit (Fig. 9C). In contrast, intervals dominated by smaller megaclasts show relatively consistent median values of D_{50} and D_{90} and maintain a more uniform thickness. The D_{50}/D_{90} ratios, reflecting the degree of sorting, generally show improved sorting downslope, with locally uniform median values within the smaller-megaclast intervals (Figs. 6E and 9C).

Fracture Data

Fractures are predominantly steeply dipping (commonly 70°–90°), display planar opening-mode (mode I) geometries, and are filled with

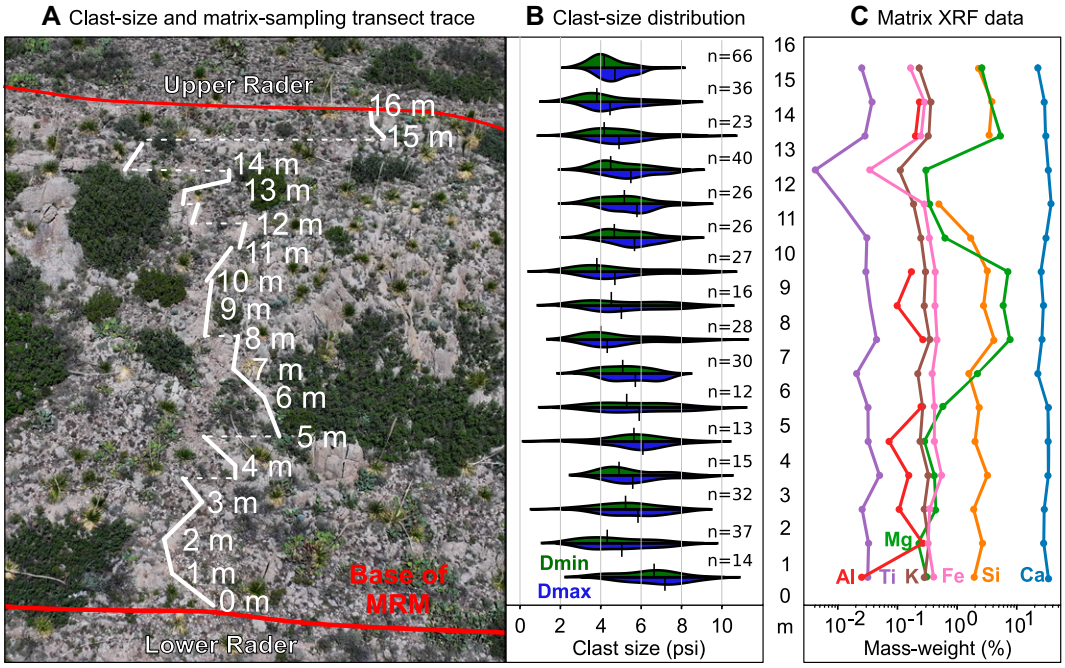


Figure 7. (A) Orthomosaic image showing a vertical transect through the middle Rader megabreccia (MRM) documenting (B) clast-size variations and (C) matrix composition. Lithoclast maximum (D_{max}) and minimum (D_{min}) apparent diameters indicate an overall fining-upward trend. The composition of the matrix is 30% Ca, with a local spike in Mg related to partial dolomitization of the matrix; the presence of Si and other terrigenous elements indicates a mixed carbonate-siliciclastic matrix. X-ray diffraction (XRD) measurements corroborate the X-ray fluorescence (XRF) data shown in part C (see text). See Figure 3 for location.

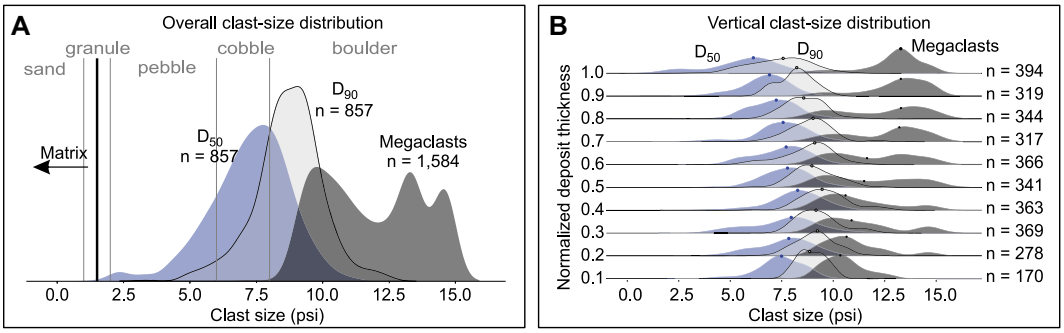


Figure 8. Clast-size distributions of the middle Rader megabreccia derived from the grid-cell dataset shown as kernel density estimations (KDEs). (A) Overall D_{50}, D_{90}, and megaclast-size distributions. (B) Vertical clast-size variability shown by normalizing the local middle Rader megabreccia thickness into 10 relative thickness intervals, accounting for lateral thickness variations (11–24 m), and allowing comparison of vertical trends independent of absolute deposit thickness. The D_{50} and D_{90} values show a slight coarsening-upward trend near the base and a strong fining-upward trend toward the top. Megaclasts show wider size variability, with an overall coarsening-upward trend. Dots indicate the median of the distributions.

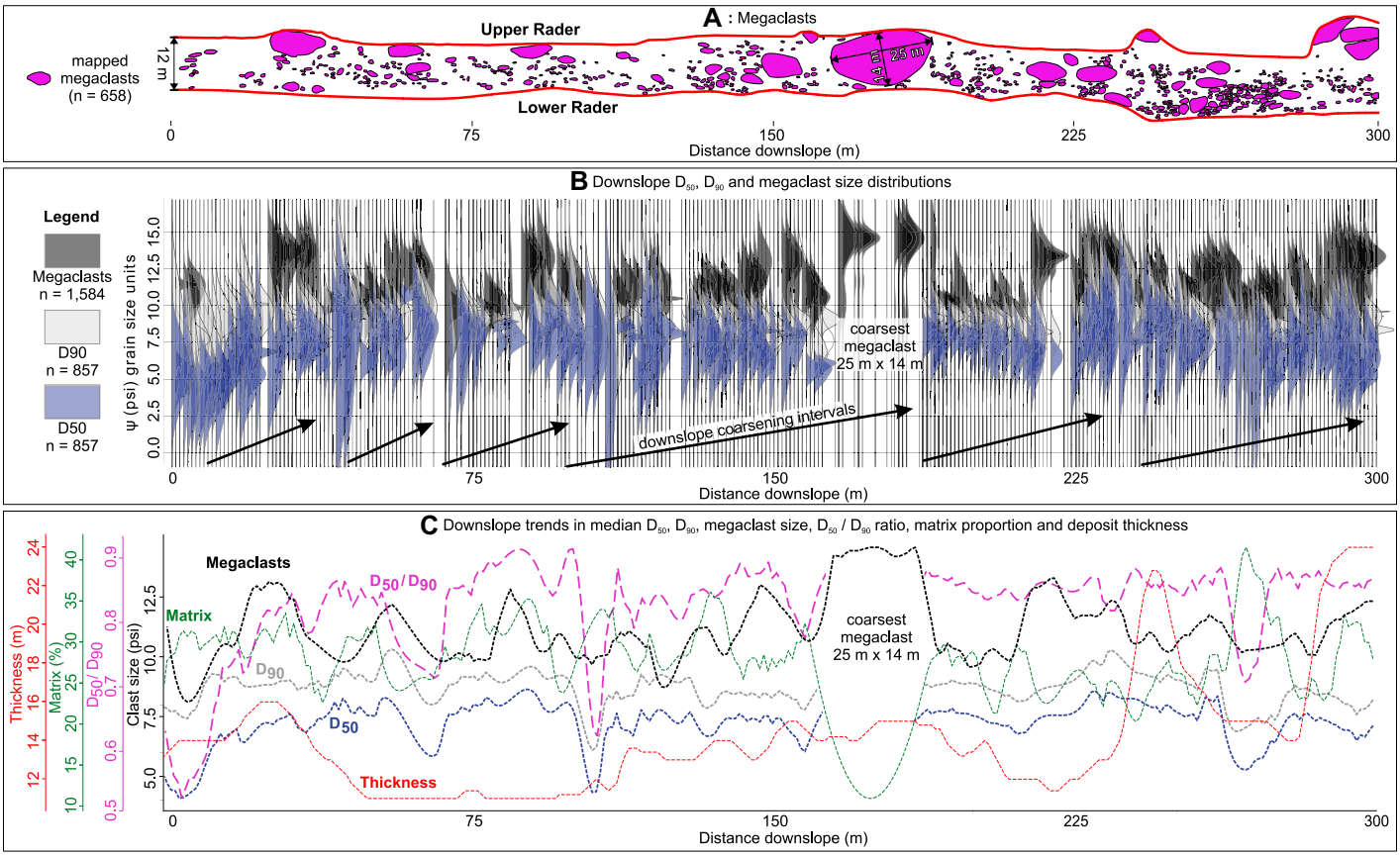


Figure 9. (A) Simplified outcrop view showing mapped megaclasts (pink polygons) and the middle Rader megabreccia boundaries (red lines). Number of mapped lithoclasts is indicated. (B) KDEs derived from the grid-cell dataset, showing distributions of D_{50}, D_{90}, and megaclast size for the combined vertical column of cells at a given downslope position. The stack of the KDEs exhibits downslope variations in distribution of D_{50}, D_{90}, and megaclast size. Sample size (n) is indicated. At some positions, no megaclasts were observed due to their absence, or lack of exposure. (C) Median values of D_{50}, D_{90}, megaclast-size, and D_{50}/D_{90} distributions. Median matrix proportion and thickness are also displayed.

blocky calcite cement. In places, fractures terminate against lithoclasts and occasionally cut through finer lithoclasts and skeletal fragments (Figs. 10A–10B). No mineralized fractures were observed to continue from the middle Rader megabreccia into the Lower Rader or Upper Rader units, nor does any fracture fully propagate from top to bottom through the entire middle Rader megabreccia, nor do any single fractures continue all the way across any megaclast. In contrast, joints that evolved from earlier fractures, as evidenced by relict calcite infill

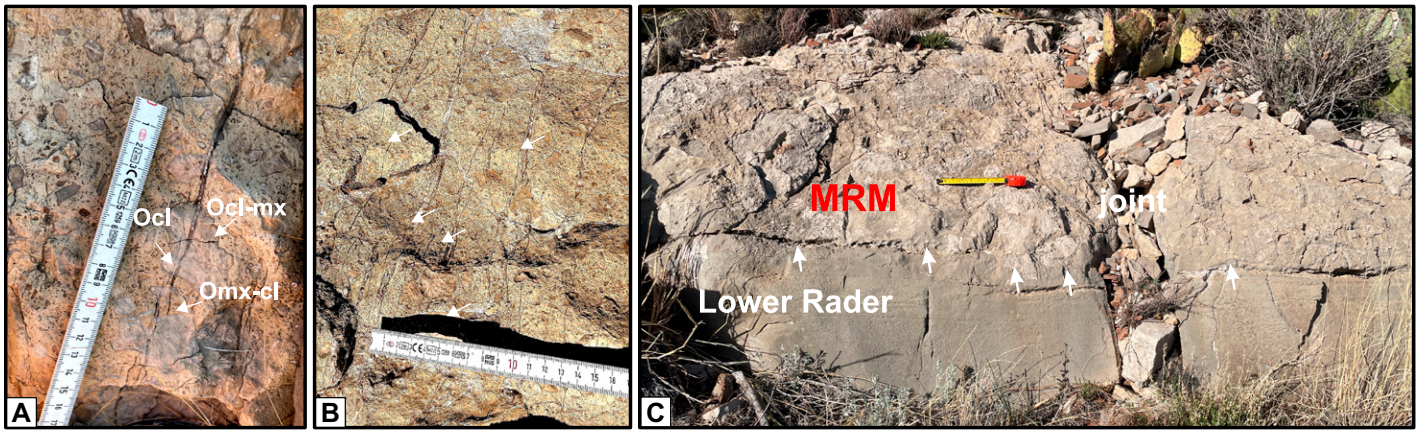


Figure 10. (A) Example of mineralized fractures in the middle Rader megabreccia (MRM). See Figure 4 for abbreviations. (B) Fracture cluster, where fractures (arrows) have approximately the same orientation. (C) Basal contact of the middle Rader megabreccia with beds of the Lower Rader submember; fractures do not propagate through this boundary, whereas a joint filled with recent surficial debris extends through the boundary.

surfaces and now filled with recent caliche and vegetation, occasionally propagate into adjacent strata.

Across all fracture collection methods, the scan-line (1), clast-bound (3B), and grid-cell (4) datasets yielded comparable fracture dimensions (Fig. 11; Table 2). In contrast, the targeted single fractures (3A) measured directly in the outcrop and those extracted from the digital outcrop model (2) represent a larger scale of observation and are therefore biased toward the largest fractures documented in the middle Rader megabreccia. Despite differences in fracture dimensions between datasets, all datasets consistently document two distinct fracture sets with similar orientations (Fig. 11). The dominant set 1 comprises fractures striking NE-SW (mean 055°), whereas set 2 strikes NW-SE (mean 150°).

Set 1 fractures are generally larger than set 2 fractures, particularly in terms of height and upper-percentile values (Fig. 11; Table 2). Median fracture heights across datasets are comparable between sets (0.11–0.50 m for set 1 and 0.08–0.50 m for set 2), with set 1 consistently showing higher P90 heights. Median lengths range 0.08–0.44 m for set 1 and 0.12–0.24 m for set 2, indicating similar median values but a broader upper range for set 1. Median fracture lengths exceed median heights for both sets, consistent with aspect ratios greater than one and indicating that fractures are typically longer than tall. Maximum apertures are comparable between sets, with median values ranging from 0.20 mm to 0.55 mm. Scanline–derived spacing and Terzaghi-corrected intensity (Terzaghi, 1965) further distinguish the two sets: Set 1 shows wider median spacing (0.22 m) and lower median intensity (4.52 fractures/m), whereas set 2 shows closer median spacing (0.18 m) and higher median intensity (5.66 fractures/m; Table 2).

In total, 16 fracture terminus types (defined in Fig. 4) were classified into five groups based on combinations of fracture-tip relationships (Fig. 12): fracture-related, clast-related, matrix-related, clast-matrix boundary–related, and undefined groups. The matrix-related group is the most common (54%), dominated by fractures terminating within the matrix at both ends (30%). The clast-related group represents 16% of all observations and is dominated by clast-bound (7%) and clast-to-clast (5%) terminus types. The fracture-related group accounts for 10%, with fracture-to-matrix (4.6%) and fracture-to-fracture (2.2%) as the most abundant terminus types within the group. The clast-matrix boundary–related group is the least frequent classified group, comprising only 4.6%, dominated by fractures terminating at clast boundaries from the matrix at both ends (3.4%). The undefined group accounts for 15% of all observations, where terminus type could not be determined due to limited exposure.

Across terminus types, overall distribution shapes are broadly comparable, but systematic differences between fracture sets are evident. Height distributions (Fig. 12A) show larger median values and a wider spread for set 1 (median ~0.12 m) than for set 2 fractures (median ~0.08 m), particularly within matrix-related and clast-matrix boundary–related groups. In contrast, length distributions (Fig. 12B) indicate that median lengths are slightly greater for set 2 fractures (~0.18 m) than for set 1 fractures (~0.15 m). Aspect ratios (Fig. 12C) consistently exceed unity, showing that fractures are generally longer than tall (median ~1.4–1.8), with set 2 exhibiting the most elongated geometries. Maximum aperture distributions (Fig. 12D) show only minor differences between sets, with set 1 displaying slightly greater variability, particularly within the matrix-related terminations group. Overall, the group of matrix-related terminations exhibits the widest distributions across all fracture dimensions, whereas the group of clast-related terminations tends to show more restricted ranges.

Spatial Fracture-Dimension Distribution

The vertical distribution of fracture dimensions (Fig. 13) is much more homogeneous compared to the clast-size vertical distribution (Fig. 8B), with fracture maximum apertures, heights, and lengths only slightly increasing from the base to the middle of the megabreccia (Fig. 13). In the upper half of the megabreccia, fracture dimensions are more consistent.

Fracture dimensions consistently decrease downslope with minor local positive deviations (Fig. 14B). The most prominent shift in fracture dimensions occurs across the largest 25 × 14 m megaclast (175–220 m), which also marks a major downslope change in lithoclast-size distribution (Figs. 9 and 14A). Upslope of this exceptional megaclast (0–200 m in Fig. 9), fracture dimensions display a wide range with fluctuating median values (Figs. 14A and 14C). In contrast, immediately downslope of the megaclast (225–300 m), fracture dimensions initially decrease with minor variability over the first ~30 m distance before systematically increasing in both magnitude and range toward the distal end of the panel (~225–300 m). Similar to the clast-size distribution, no trends were observed for fracture dimensions relative to exposure thickness and matrix content (Fig. 14C).

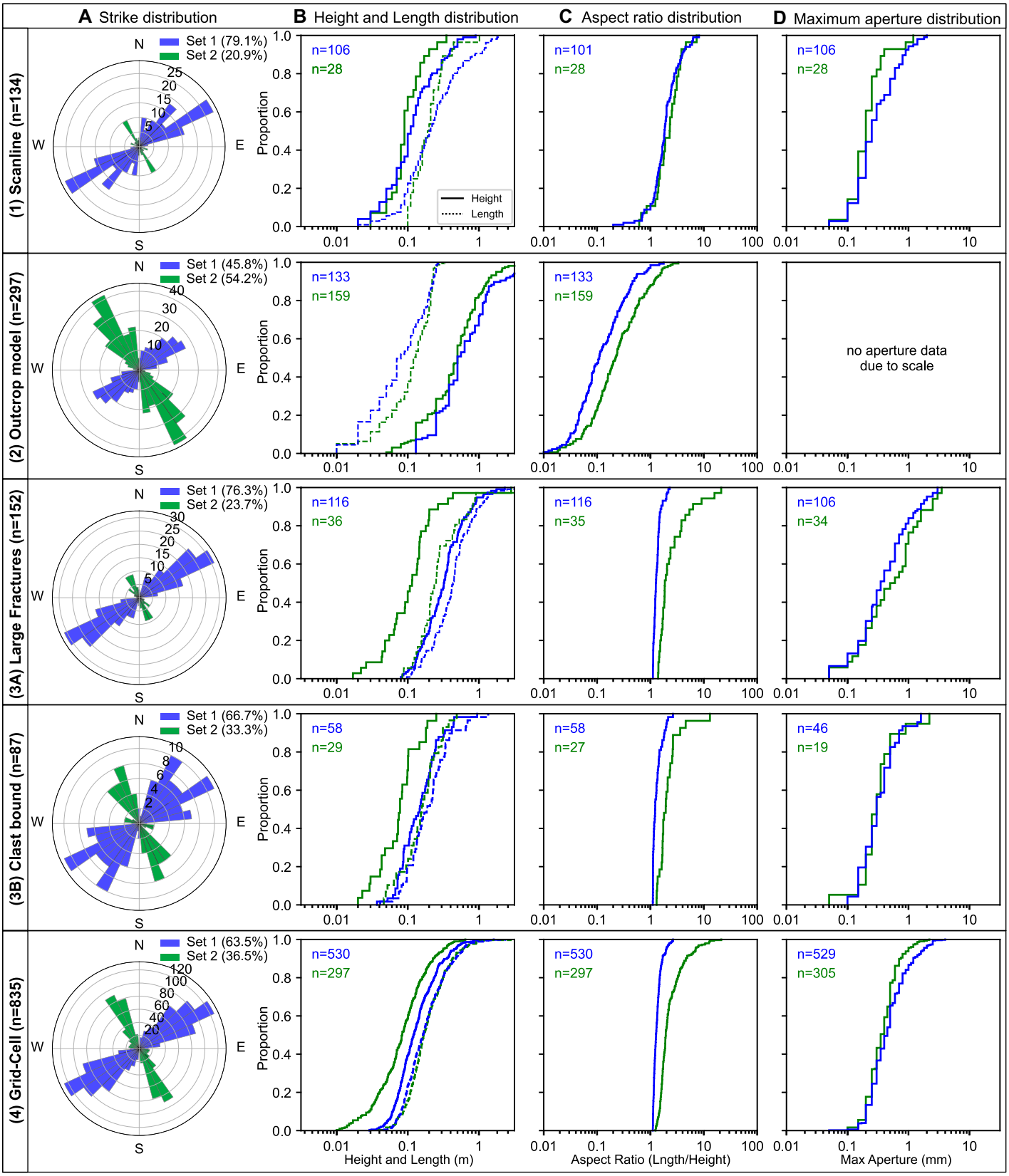


Figure 11. Fracture properties by set across data collection methods. (A) Rose diagrams showing strike distributions color-coded by fracture set. (B–D) Empirical cumulative distribution functions display the distributions of (B) fracture height (solid lines) and fracture length (dashed lines), (C) aspect ratio (i.e., length/height), and (D) maximum aperture.

TABLE 2. SUMMARY TABLE OF FRACTURE PROPERTIES FOR TWO FRACTURE SETS COLLECTED FROM THE MIDDLE RADER MEGABRECCIA (BELL CANYON, GUADALUPE MOUNTAINS, WEST TEXAS, USA) ACROSS DATA COLLECTION METHODS

Dataset	Fracture properties	P_{10}		P_{50}		P_{90}	
		Set 1	Set 2	Set 1	Set 2	Set 1	Set 2
Method 1: Scan line	Height (m)	0.04	0.05	0.11	0.09	0.38	0.18
	Length (m)	0.08	0.11	0.20	0.20	0.84	0.34
	Maximum aperture (mm)	0.10	0.10	0.25	0.20	0.85	0.37
	Spacing (m)	0.13	0.14	0.22	0.18	0.30	0.28
	Intensity (fractures/m)	3.38	3.61	4.52	5.66	7.44	6.98
Method 2: Outcrop model	Height (m)	0.25	0.13	0.50	0.50	1.82	1.34
	Length (m)	0.02	0.03	0.08	0.12	0.23	0.22
Method 3A: Large fractures	Height (m)	0.13	0.04	0.32	0.12	0.81	0.24
	Length (m)	0.16	0.13	0.44	0.24	0.99	0.79
	Maximum aperture (mm)	0.1	0.13	0.35	0.55	1.60	2.23
Method 3B: Clast bound	Height (m)	0.07	0.03	0.15	0.08	0.32	0.18
	Length (m)	0.08	0.06	0.19	0.16	0.40	0.31
	Maximum aperture (mm)	0.15	0.19	0.30	0.30	0.70	0.58
Method 4: Grid cell	Height (m)	0.06	0.03	0.12	0.08	0.35	0.23
	Length (m)	0.08	0.09	0.16	0.17	0.47	0.43
	Maximum aperture (mm)	0.20	0.20	0.45	0.35	1.20	0.73

Note: The 10th, 50th (median), and 90th percentiles (P_{10}, P_{50}, P_{90}) for each fracture property are reported. Fracture spacing and intensity were estimated exclusively from the scan-line dataset using the method of Terzaghi (1965).

Relationships Between Clast Size and Fracture Dimensions

No statistically robust relationships were observed between fracture dimensions and lithoclast-size parameters (D_{50}, D_{90}) or matrix proportion for either the clast-to-clast (Ocl-Ocl) or matrix-to-matrix (Omx-Omx) fracture types (Fig. 15). Coefficients of determination are consistently low across all panels ($R^2 = 0.00$–0.05), except for matrix proportion versus maximum aperture in the Omx-Omx type ($R^2 = 0.15$; Fig. 15D), which represents the strongest signal in the figure but remains a weak relationship.

Similarly, no robust relationships were observed between clast diameters and clast-bound fracture dimensions at the scale of individual clasts (Fig. 16). The highest observed relationships included a weak positive trend between

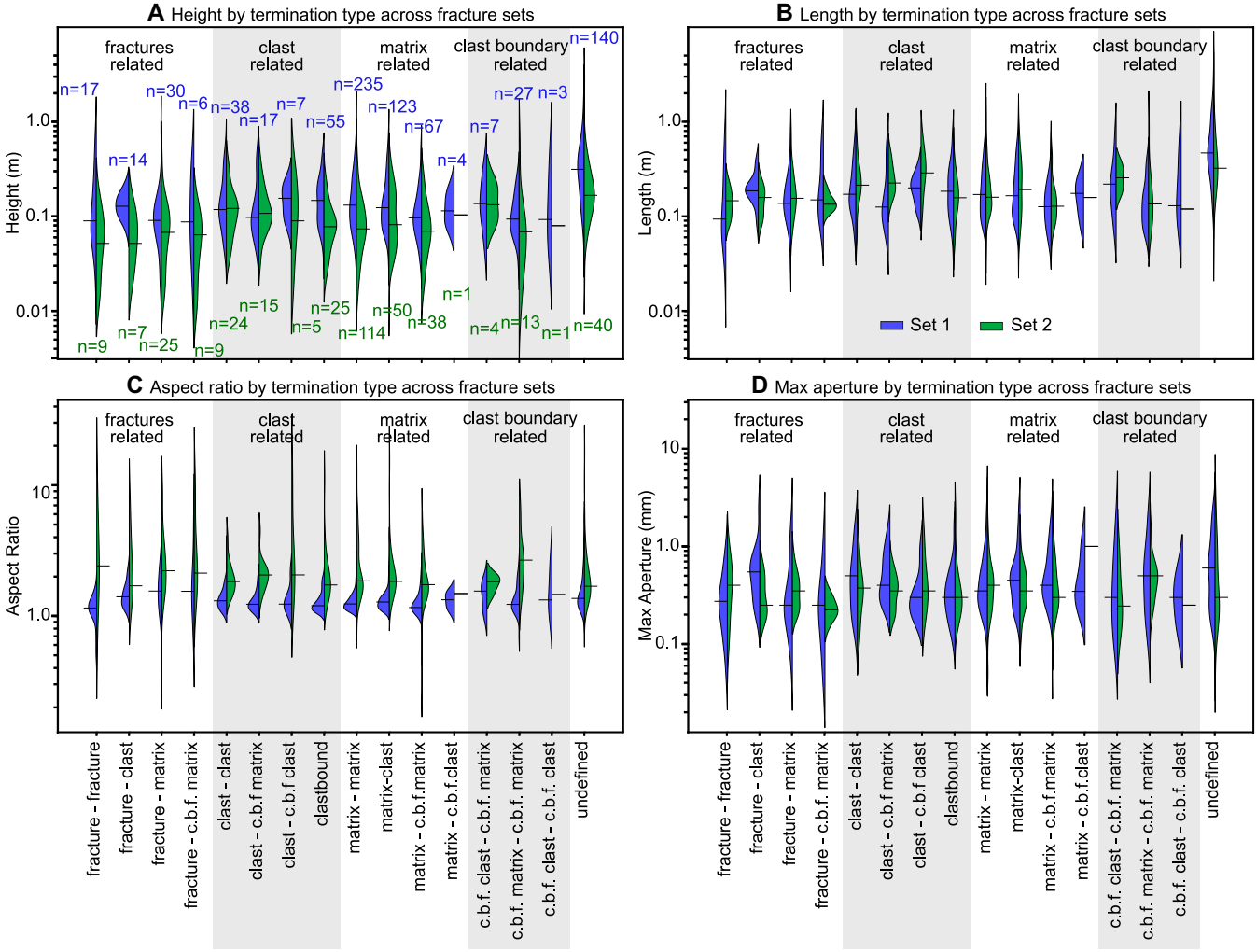


Figure 12. Kernel density estimations derived from the grid-cell, scan-line, targeted large fractures, and targeted clast-bound datasets, showing distributions of fracture (A) height, (B) length, (C) aspect ratio, and (D) maximum aperture by sets across terminus types. Sample size (*n*) for each terminus type is indicated. See Figure 4 for definitions of terminus types. c.b.f.—clast boundary from.

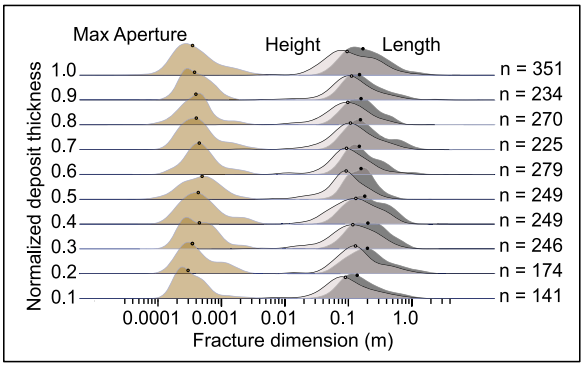


Figure 13. Kernel density estimations derived from the grid-cell dataset, showing distributions of fracture maximum aperture, height, and length at each normalized middle Rader megabreccia thickness interval (see also Fig. 8B). Sample size (*n*) for each interval is indicated at right. Dots indicate the median of the distributions. Fracture dimensions slightly increase from the base to the middle of the middle Rader megabreccia but then remain consistent throughout the upper half of the middle Rader megabreccia.

clast maximum apparent diameter and fracture height ($R^2 = 0.11$; Fig. 16A), and between clast minimum apparent diameter and fracture maximum aperture ($R^2 = 0.16$; Fig. 16D).

DISCUSSION

The 20-m thick, 300-m long, oblique-dip–oriented outcrop that is the focus of this study exposes a localized portion of the 13-km-long middle Rader megabreccia and thus may not capture the full dip- and strike-oriented variability of the unit across the Guadalupe Mountains. However, this study provides quantified constraints on the sedimentology and depositional mechanisms of the middle Rader megabreccia. Integration of these sedimentological data with our large ($n = 1514$) fracture dataset provides a robust example for analyzing fracture stratigraphy in carbonate toe-of-slope breccias. Unless otherwise stated, the fracture interpretations presented here refer specifically to mineralized fractures and do not include late-stage, nonmineralized joints measured in the outcrop model.

Emplacement Mechanism for the Middle Rader Megabreccia

The middle Rader megabreccia is composed primarily of lithoclasts derived from outer-shelf and reefal settings (e.g., packstones and

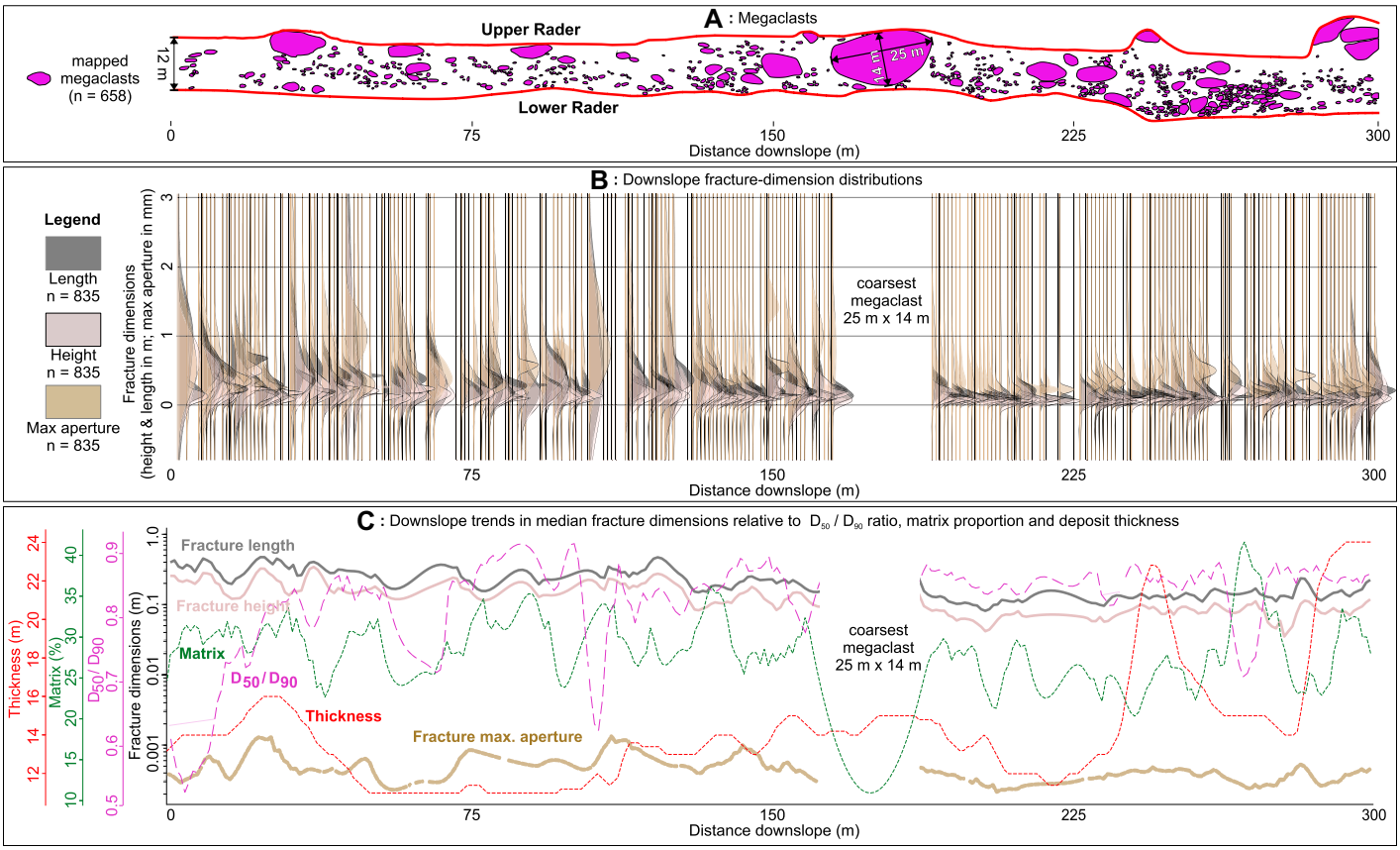


Figure 14. (A) Simplified outcrop view showing mapped megaclasts (pink polygons) and the middle Rader megabreccia boundaries (red lines). Number of mapped lithoclasts is indicated. (B) Kernel density estimations derived from the grid-cell dataset, showing distributions of fracture dimensions for the combined vertical column of cells at a given downslope position. The stack of the KDEs exhibits downslope variations in the distribution of fracture length, height, and maximum aperture. Sample size (*n*) is indicated. At some positions, no fractures were observed due to lack of exposure. (C) Median values of fracture length, height, and maximum aperture distributions. Median matrix proportion and thickness are also displayed. Kernel density estimates are shown for visualization only; minor density extending into negative values reflects kernel smoothing artifacts near zero and does not indicate negative fracture dimensions.

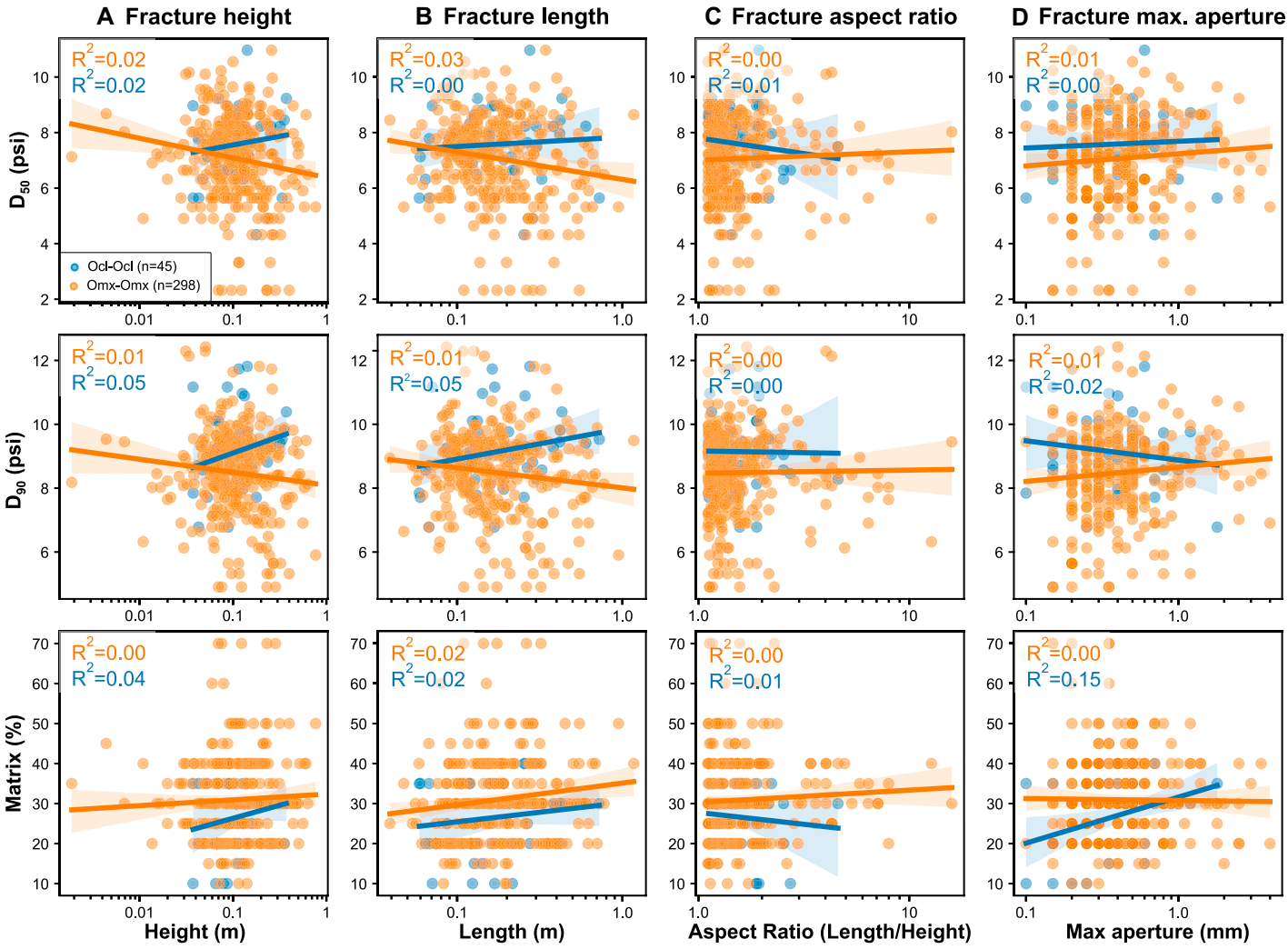


Figure 15. Scatter plots showing relationships between fracture dimensions, including (A) height, (B) length, (C) aspect ratio, and (D) maximum aperture, vs. clast size (D_{50} and D_{90}) and matrix proportion across clast-to-clast (Ocl-Ocl) and matrix-to-matrix (Omx-Omx) terminus types. The straight lines and shaded polygons represent best-fit regressions and confidence intervals, color-coded by fracture terminus type. Color-coded coefficients of determination indicate consistently absent relationships between fracture dimensions and clast size (typically R^2 = ~0.00–0.05).

boundstones containing *Polydiexodina*, *Tubiphytes*, and *Archaeolithoporella*; Fig. 6), as also noted by Lawson (1989). These clasts were lithified prior to failure, particularly the boundstone facies, which promoted brittle margin collapse, generating coherent blocks rather than soft-sediment slumps (sensu Playton et al., 2010). One such megablock is preserved along the outcrop panel (Fig. 9), with exposed dimensions of ~14 × 25 m, although its original geometry was likely modified during downslope translation (e.g., Zhang et al., 2023). The presence of siliciclastic lithoclasts (occasionally preserving bedding in meter-scale structures; Fig. 5E) suggests rip-up clasts and incorporation of lower-slope to toe-of-slope strata into this mass flow.

The mixed siliciclastic-carbonate nature of the matrix between lithoclasts indicates that the mass flow entrained both loose skeletal material (e.g., fusulinid; Fig. 5G) and siliciclastic sediment eroded from outer-shelf to lower-slope settings. Enrichment of the matrix in detrital elements (Al, Si, K, Ti, Fe), particularly in the basal part of the megabreccia (Fig. 7), further implies disaggregation of siliciclastic rip-up clasts during transport, contributing to the mixed siliciclastic-carbonate composition of the megabreccia matrix. Dynamic disintegration (i.e., clasts breaking into smaller pieces) and frictional abrasion (i.e., rounding) may reduce the volume of individual particles within such mass flows by several orders of magnitude from source to deposit (Locat et al., 2006; De Blasio and Crosta, 2015), progressively contributing to the finer-grained fraction. Particle-size analysis of analogous deposits demonstrated that fragmentation continues during runout, progressively increasing the proportion of fine particles with distance (Dufresne and Dunning, 2017; Marc et al., 2021). This transition from boulder-rich to granule-dominated flows progressively alters the internal framework of the moving mass, filling the pore spaces between larger clasts and reducing internal frictions (e.g., Davies and McSaveney, 2009).

The megaclasts are preferentially deposited near the top of the middle Rader megabreccia, while the vertical trend in D_{50} and D_{90} distributions (Fig. 8B) shows inverse grading in the basal third, transitioning upward into normal

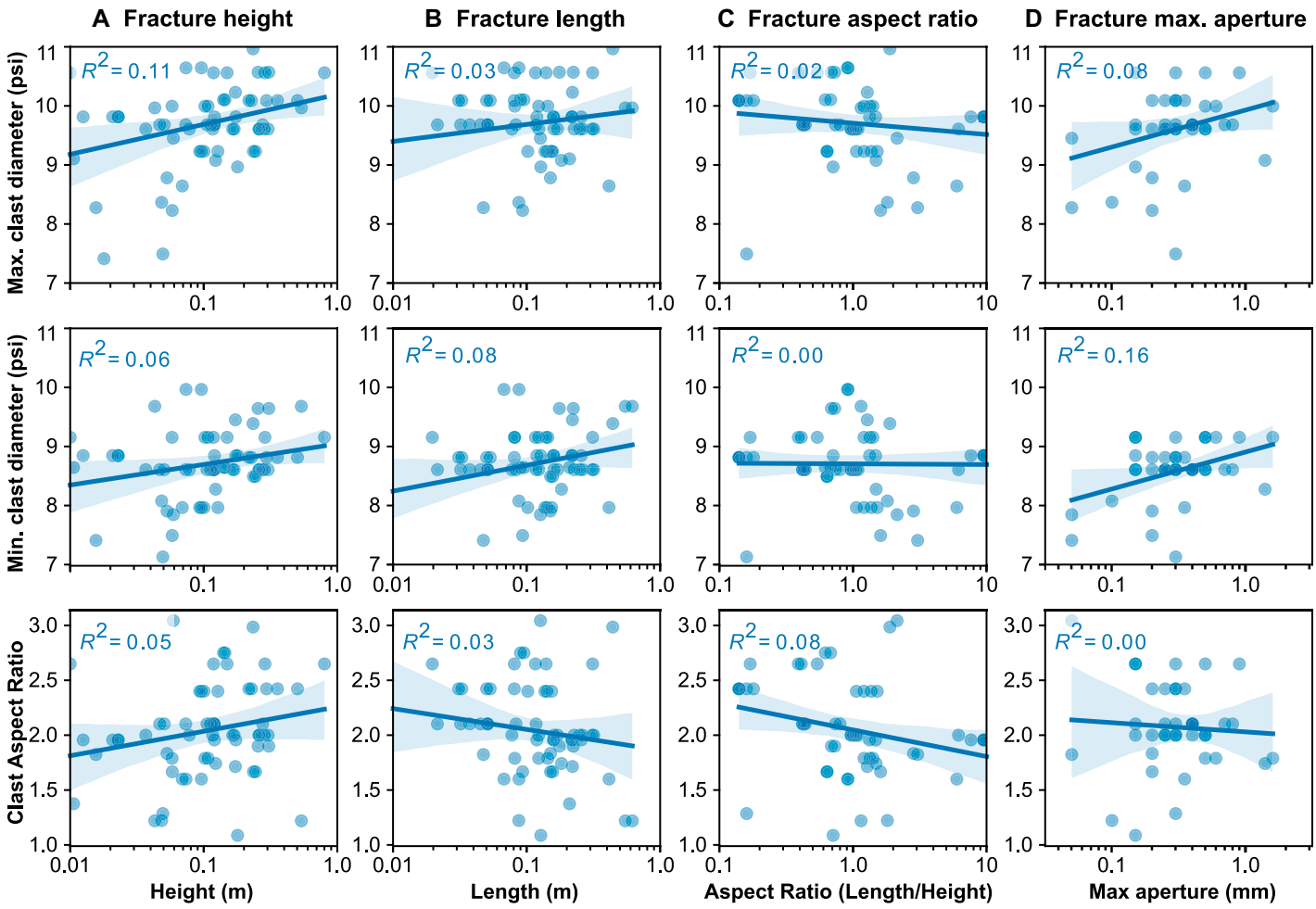


Figure 16. Scatter plots showing relationships between fracture dimensions, including (A) height, (B) length, (C) aspect ratio, and (D) maximum aperture, vs. minimum and maximum lithoclast diameters and aspect ratios (maximum/minimum apparent diameters), for clast-bound fractures (n = 63). The straight lines and shaded polygons represent best-fit regressions and confidence intervals, respectively. Coefficients of determination (R^2) indicate generally absent relationships between fracture dimensions and clast size or shape.

grading. Although such size grading may reflect a cohesive flow structure (Iverson, 1997), this is unlikely for the middle Rader megabreccia given the scarcity of cohesive clay in the matrix, abundance of lithoclasts relative to matrix material, and the absence of ductile deformation fabrics (cf. Simabrata et al., 2025). Instead, the observed vertical grading together with inferred sediment dynamics, subangular to subrounded clast shape, and overall clast-supported fabric more plausibly reflect granular segregation driven by dispersive pressure and kinetic sieving (Middleton, 1970; Savage and Lun, 1988; Mullin, 2000; Gray, 2018). These are processes characteristic of granular flows (Sallenger, 1979; Nemec, 1990; Gray, 2018).

Within granular flows, frequent particle collisions act to fragment clasts by dynamic disintegration, with preexisting joints and fractures strongly controlling breakage pathways (Weidinger et al., 2014; Dufresne et al., 2016; Magnarini et al., 2021), while frictional abrasion contributes to the rounding of the lithoclasts and bioclasts and also generates fine matrix particles (Perinotto et al., 2015). During downslope movement, finer particles percolate downward due to kinetic sieving (Middleton, 1970) while larger clasts are driven upward by dispersive pressure (Sallenger, 1979; Savage and Lun, 1988), producing inverse grading in the coarse tail of the distribution (D_{90}), whereas finer particles remain broadly distributed throughout the flow depth (Gray and Ancey, 2011). Progressive enrichment in fines reduces interparticle friction and enhances flow mobility, thereby facilitating longer runout distances (Kokelaar et al., 2014).

Laterally, the faster-moving top of the flow concentrates coarser clasts at the flow front, where they frictionally interact with substrate sediment that resists the flow motion (Vallance and Savage, 2000). This resistance forms a bulbous-shaped flow head, capable of eroding the substrate, depositing on top of it, fragmenting megaclasts, and reincorporating these fragments into the moving mass. Locally within the flow, large megablocks that move more slowly than the surrounding granular mass can act as obstacles. Faster-moving, clast-rich portions of the flow impinge on these slower megablocks, increasing particle collisions and granular stresses and generating a compressed "shock zone" upstream of the block (e.g., Yang et al., 2020). In this zone, coarse clasts become trapped, producing local thickening and a rise in the free upper boundary of the flow. Meanwhile, the more mobile finer clasts are forced to divert laterally, upward, or through pore spaces between larger clasts. Immediately downstream of the slower-moving blocks, the flow transitions into a more dilute and mobile regime as mate-

rial bypasses the obstacle (e.g., Cui et al., 2022). Such obstacle-controlled reorganization of flow structure and grain-size distribution explains the observed drop in the elevation of the middle Rader megabreccia top and the concurrent decrease in clast size immediately downslope of the largest megaclast (25 × 14 m; Fig. 9 at ∼170 m downslope). Such coarse-grained granular flows have been reported to form levees during transport by the "shouldering aside" of megaclasts, while the finer material advances as a central core of the flow (e.g., Johnson et al., 2012). Although the exposure is insufficient to identify and map these detailed variations, modern subaerial (e.g., Hoblitt, 1986; Kokelaar et al., 2014) and experimental analogs (e.g., Johnson et al., 2012; Baker et al., 2016) indicate that these geometries are common.

To summarize, the consistent vertical grading of the D_{50} and D_{90} distributions and the presence of megaclasts near the top of the middle Rader megabreccia suggest that the studied deposit within our 300 m detailed window was emplaced by a single grain-flow event. The coarsening cycles of megaclast size observed in the downslope direction (Fig. 9B) are interpreted to reflect deposition from surges within a single flow event rather than resulting from multiple flow events (e.g., Arai et al., 2013; Aaron et al., 2025). The lack of laterally extensive internal surfaces further supports the interpretation of a single event. Importantly, the middle Rader megabreccia in other locales shows evidence of multiple flow events (Lawson, 1989). We therefore interpret our study area (Fig. 3) to represent the distal expression of a single flow event within the "Middle Rader Stage 2" depositional phase of Playton et al. (2025b), but we acknowledge that the middle Rader megabreccia shows clear evidence in other locales as the amalgamated deposit of multiple events.

Timing of Fracture Formation

The predominance of steep fracture dips (commonly 70°–90°), together with the absence of observable shear displacement, indicates that fractures formed by opening-mode (mode I) extensional stresses (Schultz, 2019). Fractures display predominantly planar geometries and smooth fracture surfaces, lacking the irregular, nonplanar forms and rough morphologies typical of syndepositional fractures formed under low differential stress (cf. Narr et al., 2024). The common blocky calcite cement fill of the fractures, coupled with the absence of fibrous or radiaxial marine calcite, sediment fill, or microbial encrustation, also argues against a syndepositional or shallow-marine fracture origin and instead suggests fracture opening and sealing under burial or tectonic conditions (Koša and Hunt, 2005; Narr et al., 2024; Ferrill et al., 2024). No fracture networks attributable to pretransport syndepositional deformation were observed within individual megaclasts, suggesting that any preexisting (i.e., syndepositional) fractures were likely deformed during transport by frequent particle collisions and dynamic disintegration in the granular flow (Weidinger et al., 2014; Dufresne et al., 2016; Magnarini et al., 2021). This interpretation is consistent with subsurface and outcrop studies showing that syndepositional fractures are mainly concentrated on the outer shelf, reef, and upper slope (e.g., Narr et al., 2024; Playton et al., 2025c).

Two suborthogonal fracture sets with comparable spacing suggest progressive extensional jointing rather than synchronous fracture formation (Bons et al., 2012). Initial mode I fractures formed perpendicular to the minimum compressive stress under elevated fluid pressure, promoting tensile failure and opening. The formation and sufficient sealing of this early fracture set likely altered the mechanical behavior of the breccia by redistributing the local effective stress field (Ramsay, 1980). Continued loading, elevated pore-fluid pressure, and reorganization of the regional stress could have subsequently promoted the development of a second mode I fracture set. Constraints on the relative timing of these fracture sets are limited (cf. Aditama et al., 2026) by the small number of fractures terminating against other fractures (Fig. 12) and cannot be resolved from the available data alone. However, a recent study of the Lamar Member along U.S. Highway 62 documented orthogonal sets of near-vertical opening-mode veins with strike orientations comparable to those observed here (Ferrill et al., 2024). Fluid inclusion microthermometry indicates that NE-striking veins (equivalent to set 1) record greater maximum trapping depths (∼3.6–4.5 km) than NW-striking veins (equivalent to set 2; ∼2.7–3.4 km), suggesting set 1 formed earlier under deeper burial conditions. Based on vein orientations and regional structural context, Ferrill et al. (2024) interpreted these fractures as forming under burial conditions from basinal fluids, with set 1 reflecting post-Laramide stress relaxation and set 2 associated with the onset of Basin-and-Range extension. Alternatively, the fracture sets could be interpreted as a conjugate pair, but conjugate fracture geometries are uncommon in mode I systems and typically require shear or hybrid fracture modes (Bons et al., 2012).

Factors Influencing Fracture Dimensions

Fractures in the middle Rader megabreccia are generally small, with median height of 13 cm and median length of 20 cm (Fig. 11). However, the presence of larger fractures with maximum height and length of 2.84 m and 4.12 m, respectively (with undefined termini, extending beyond the exposed outcrop or into cover), suggests that some fractures have the potential for further propagation. Despite this, no mineralized fractures cutting through the entire thickness of the middle Rader megabreccia were observed, nor fractures fully propagating through any single megaclast, indicating strong vertical propagation limits, which is further supported by the consistent dominance of the fracture length over height (Table 2). This vertical limit may be related to an inherent mechanical barrier within the megabreccia, potentially associated with the concentration of megaclasts toward the top of the middle Rader megabreccia.

Further analysis of the spatial distribution of fracture dimensions (Fig. 14) revealed a subtle downslope decrease in fracture length, height, and maximum aperture, with wider variability proximally than distally. However, this downslope pattern in fracture dimensions does not represent a simple proximal-distal gradient; instead, it probably reflects local changes in internal breccia heterogeneity (Brace et al., 1966), potentially related to local variations in clast sorting (see D_{50}/D_{90} curve in Fig. 14C). The most pronounced clast-size influence on fracture dimensions occurs across the largest mapped megaclast (25 × 14 m at ∼170 m downslope; Fig. 14). Immediately upslope from this megaclast, fractures are larger (median lengths ∼0.25 m and heights ∼0.15 m) and more variable within an ∼40 m upslope interval, coinciding with an interval of coarser-clast accumulation. In contrast, fracture dimensions immediately downslope from the megaclast are smaller (median lengths ∼0.10 m and heights ∼0.05 m) and show less variability over ∼40 m distance, coinciding with an interval dominated by finer megaclasts.

Within this outcrop-scale mechanical framework, the observed fracture termination patterns (Fig. 12) provide direct, quantitative evidence for heterogeneity-controlled fracture growth. The high proportion of matrix-hosted fracture terminations (Omx–Omx: 30%), compared to the low frequency of clast-confined terminations (Ocl–Ocl: 5%), indicates that the matrix was mechanically weaker and favored fracture propagation, while clasts acted as competent elements that inhibited fracture growth. Fractures propagating from the matrix and terminating at clast boundaries, whether at both ends (Omx-cl–Omx-cl: 3.4%) or at least one end (Omx–Omx-cl, Ocl–Omx-cl, and F–Omx-cl: 13.1%), further indicate that stiffness contrasts and interfacial weaknesses at clast margins acted as effective

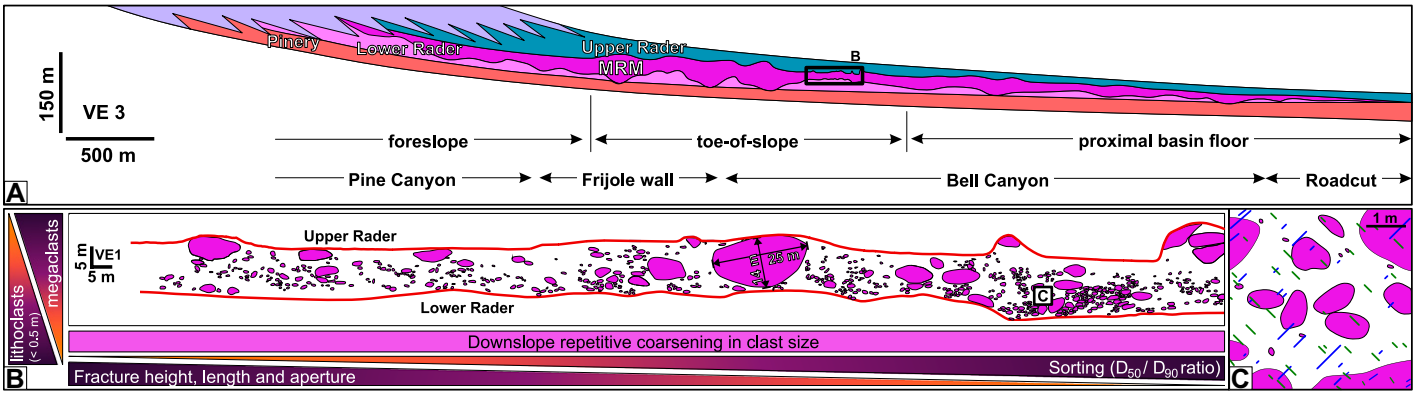


Figure 17. Schematic summary of the sedimentology and fracture stratigraphy of the middle Rader megabreccia (MRM; Bell Canyon Formation, Guadalupe Mountains, Texas, USA). (A) Depositional model illustrating the lower-slope, toe-of-slope, and proximal basin-floor settings, showing the stratigraphic relationships of the Pinery Member and the Lower, Middle, and Upper Rader submembers, modified from Playton et al. (2025b). VE—vertical exaggeration. (B) Simplified outcrop panel highlighting the lower and upper boundaries of the middle Rader megabreccia and the mapped distribution of megaclasts. The approximate depositional position is indicated in part A by a black box. (C) Stochastically generated schematic illustration (location shown in part B) of fracture distribution showing set 1 (blue) and set 2 (green) based on their orientations and characteristic dimensions.

barriers to fracture growth, promoting fracture arrest or deflection rather than transmission into clasts. These observations are consistent with other studies showing that fracture localization in heterogeneous materials is governed by the abundance of grain boundaries and interfaces, such that finer-grained matrix domains characterized by abundant matrix–clast contacts promote more extensive fracture initiation than mechanically coherent clasts (Fredrich et al., 1990; Zhang et al., 2019). Together with shear remolding, clay enrichment, and internal compartmentalization reported for submarine mass-transport deposits (Cardona et al., 2022; Simabrata et al., 2025), these features enhance mechanical anisotropy and reduce permeability, causing such deposits to function as seals rather than reservoir intervals in the subsurface.

Despite the spatial associations described in the previous two paragraphs, statistical relationships between fracture dimensions and clast-size metrics are not robust (Figs. 15 and 16), likely reflecting the combined influence of multiple controls operating at different scales, including local mechanical contrasts, dolomitization, stress distribution, and/or clast–matrix interfaces, rather than a single dominant parameter. In addition, estimated clast-size metrics for a given grid cell do not necessarily correspond directly to the specific fractures measured within that cell, as fracture measurements and clast-size estimations were conducted using distinct sampling approaches and represent separate spatial scales (see Methods for details). Furthermore, both fracture and clast-size measurements were derived from 2-D outcrop exposures, which may not fully represent the actual 3-D geometry and volume distribution of fractures and clasts. These methodological limitations may obscure relationships between clast size and fracture dimensions and therefore might contribute to the observed scatter. Future studies integrating higher-resolution measurements that directly link individual fractures to their host and/or surrounding clasts, as well as expanded datasets across multiple outcrops, are needed to more rigorously evaluate these relationships.

Fracture Stratigraphy of the Middle Rader Megabreccia

Fracture stratigraphy within the middle Rader megabreccia reflects the overprinting of fracturing onto an exceptionally heterogeneous depositional framework defined by extreme variability in clast size, mixed matrix composition, and spatial thickness (Fig. 17A). The internal organization of the deposit, characterized by inverse grading of megaclasts (>0.5 m in diameter), likely acts as a vertical mechanical constraint that limits vertical fracture propagation (Fig. 17B). Downslope variations in fracture dimensions reflect mechanical heterogeneity, where lithoclasts act as fracture-propagation–impeding inclusions, and their clast-size variability amplifies these mechanical contrasts. These contrasts are a direct consequence of the granular-flow emplacement mechanism, which established the clast-size organization and mechanical framework of the deposit. Collectively, these observations demonstrate that toe-of-slope carbonate megabreccias are inherently prone to small, poorly connected fracture networks (Fig. 17C), implying that subsurface megabreccia deposits similar to the middle Rader megabreccia are likely to present significant challenges for reservoir connectivity, flow efficiency, and predictability (e.g., Tengiz, Kazakhstan; Playton et al., 2025c).

CONCLUSIONS

The middle Rader megabreccia is a toe-of-slope carbonate lithoclast-supported breccia deposit in which depositional architecture and fracture development are fundamentally linked through extreme textural variability that drives fracture distribution. Such textural variability reflects emplacement by a single long-runout granular mass flow sourced from lithified reef and outer-shelf carbonates with locally entrained siliciclastic sediment, in which granular segregation (kinetic sieving and dispersive pressure) produced inverse grading, internal megablocks controlled lateral grain-size variations, and clast fragmentation together with abrasion generated matrix fines enrichment during downslope transport. The inverse grading of megaclasts within the megabreccia imposes vertical mechanical constraints, resulting in vertically confined fractures, indicating architectural control on fracture geometry. Lateral clast-size organization further controls downslope fracture dimensions, with coarser, more heterogeneous intervals hosting larger and more variable fractures, demonstrating internal textural control on fracture dimensions. Preferential fracture propagation within the matrix of the megabreccia and frequent arrest or deflection at clast boundaries and within lithoclasts show that clasts act as mechanically competent inclusions, indicating that grain–matrix

stiffness contrasts govern fracture growth. Together, these observations illustrate how depositional processes impact fracture distribution in debris-dominated carbonate toe-of-slope systems. These results provide a robust outcrop analogue demonstrating why fracture-enhanced permeability in carbonate toe-of-slope megabreccias is inherently localized and difficult to upscale, and they underscore the necessity of explicitly incorporating clast architecture and mechanical heterogeneity into reservoir models of debris-dominated carbonate.

ACKNOWLEDGMENTS

We are grateful to Chevron Corporation and Tengizchevroil for funding this research and for technical guidance. Additional funding was provided by the Society for Sedimentary Geology (SEPM), West Texas Geological Society, and the Kent Fund at Colorado School of Mines. We also thank EasyCopy for granting a research license for the EasyCore software, which was used to digitize field-measured lithological logs. We sincerely appreciate the rangers and staff of the Guadalupe Mountains National Park for their invaluable support, without which this research would not have been possible. We thank reviewers Qiqi Wang and Jean Hsieh and Associate Editor Troy Rasbury for their insightful reviews, which improved the focus and clarity of the manuscript and figures. Finally, we extend our gratitude to the students and faculty at Nazarbayev University in Astana, Kazakhstan, and the Colorado School of Mines for help with fieldwork, including Bas den Brok, Milovan Fustic, Amir Umralin, Dias Bekashov, Alisher Igizgali, Dinara Nadirkhanova, Togzhan Mynbayeva, Mary Carr, Guldana Alimzhanova, Sanzhar Begimbetov, Viska Dewi, Maximilano Miguez, Zaid Nadhim, and Sera Maurice Reyes.

REFERENCES CITED

Aaron, J., Langham, J., Spielmann, R., Hirschberg, J., McArdell, B., Boss, S., Johnson, C., and Gray, J.M., 2025, Detailed observations reveal the genesis and dynamics of destructive debris-flow surges: Communications Earth & Environment, v. 6, 556, https://doi.org/10.1038/s43247-025-02488-7.

Aditama, M.R., Hollis, C., Huuse, M., and Healy, D., 2026, Multi-scale fault and fracture networks of the UK's Mississippian carbonate platforms: Implications for extracting geothermal energy: Geothermics, v. 135, https://doi.org/10.1016/j.geothermics.2025.103513.

Amy, L.A., 2019, A review of producing fields inferred to have upslope stratigraphically trapped turbidite reservoirs: Trapping styles (pure and combined), pinch-out formation, and depositional setting: AAPG Bulletin, v. 103, p. 2861–2889, https://doi.org/10.1306/02251917408.

Arai, M., Huebl, J., and Kaitna, R., 2013, Occurrence conditions of roll waves for three grain–fluid models and comparison with results from experiments and field observation: Geophysical Journal International, v. 195, no. 3, p. 1464–1480, https://doi.org/10.1093/gji/ggt352.

Baker, J.L., Johnson, C.G., and Gray, J.M.N.T., 2016, Segregation-induced finger formation in granular free-surface flows: Journal of Fluid Mechanics, v. 809, p. 168–212, https://doi.org/10.1017/jfm.2016.673.

Barbier, M., Hamon, Y., Callot, J.-P., Floquet, M., and Daniel, J.-M., 2012, Sedimentary and diagenetic controls on the multiscale fracturing pattern of a carbonate reservoir: The Madison Formation (Sheep Mountain, Wyoming, USA): Marine and Petroleum Geology, v. 29, no. 1, p. 50–67, https://doi.org/10.1016/j.marpetgeo.2011.08.009.

Blott, S.J., and Pye, K., 2012, Particle size scales and classification of sediment types based on particle size distributions: Review and recommended procedures: Sedimentology, v. 59, p. 2071–2096, https://doi.org/10.1111/j.1365-3091.2012.01335.x.

Bons, P.D., Elburg, M.A., and Gomez-Rivas, E., 2012, A review of the formation of tectonic veins and their microstructures: Journal of Structural Geology, v. 43, p. 33–62, https://doi.org/10.1016/j.jsg.2012.07.005.

Brace, W.F., Paulding, B.W., and Scholz, C.H., 1966, Dilatancy in the fracture of crystalline rocks: Journal of Geophysical Research, v. 71, p. 3939–3953, https://doi.org/10.1029/JZ071i016p03939.

Cardona, S., Kobayashi, H., Wood, L., Dugan, B., and Milkov, A.V., 2022, Assessing the sealing quality of submarine mass transport complexes and deposits: Marine and Petroleum Geology, v. 143, https://doi.org/10.1016/j.marpetgeo.2022.105748.

Collins, J.F., Narr, W., Harris, P.M., Playton, T.E., Jenkins, S., Tankersley, T., and Kenter, J.A.M., 2014, Lithofacies, depositional environments, burial diagenesis, and dynamic field behavior in a Carboniferous slope reservoir, Tengiz Field (Republic of Kazakhstan), and comparison with outcrop analogs, *in* Verwer, K., Playton, T.E., and Harris, P.M., eds., Deposits, Architecture, and Controls of Carbonate Margin, Slope, and Basinal Settings: Society for Sedimentary Geology (SEPM) Special Publication 105, p. 50–83, https://doi.org/10.2110/sepmsp.105.11.

Cook, H.E., and Mullins, H.T., 1983, Basin margin environment, *in* Scholle, P.A., Bebout, D.G., and Moore, C.H., eds., Carbonate Depositional Environments: American Association of Petroleum Geologists Memoir 33, p. 539–618, https://doi.org/10.1306/M33429C18.

Cooke, M.L., Simó, J.A., Underwood, C.A., and Rijken, P., 2006, Mechanical stratigraphic controls on fracture patterns within carbonates and implications for groundwater flow: Sedimentary Geology, v. 184, no. 3–4, p. 225–239, https://doi.org/10.1016/j.sedgeo.2005.11.004.

Cui, X., Harris, M., Howarth, M., Zealey, D., Brown, R., and Shepherd, J., 2022, Granular flow around a cylindrical obstacle in an inclined chute: Physics of Fluids, v. 34, https://doi.org/10.1063/5.0101694.

Davies, T.R., and McSaveney, M.J., 2009, The role of rock fragmentation in the motion of large landslides: Engineering Geology, v. 109, no. 1–2, p. 67–79, https://doi.org/10.1016/j.enggeo.2008.11.004.

De Blasio, F.V., and Crosta, G.B., 2015, Fragmentation and boosting of rock falls and rock avalanches: Geophysical Research Letters, v. 42, no. 20, p. 8463–8470, https://doi.org/10.1002/2015GL064723.

Della Porta, G., Kenter, J.A.M., Bahamonde, J.R., Immenhauser, A., and Villa, E., 2003, Microbial boundstone dominated carbonate slope (Upper Carboniferous, N Spain): Microfacies, lithofacies distribution and stratal geometry: Facies, v. 49, p. 175–207, https://doi.org/10.1007/s10347-003-0031-0.

Drzewiecki, P.A., and Simó, J.A., 2002, Depositional processes, triggering mechanisms and sediment composition of carbonate gravity flow deposits: Examples from the Late Cretaceous of the south-central Pyrenees, Spain: Sedimentary Geology, v. 146, p. 155–189, https://doi.org/10.1016/S0037-0738(01)00171-3.

Dufresne, A., and Dunning, S.A., 2017, Process dependence of grain size distributions in rock avalanche deposits: Landslides, v. 14, no. 5, p. 1555–1563, https://doi.org/10.1007/s10346-017-0806-y.

Dufresne, A., Bösmeier, A., and Prager, C., 2016, Sedimentology of rock avalanche deposits—Case study and review: Earth-Science Reviews, v. 163, p. 234–259, https://doi.org/10.1016/j.earscirev.2016.10.002.

Dunham, R.J., 1962, Classification of carbonate rocks according to depositional texture, *in* Ham, W.E., ed., Classification of Carbonate Rocks—A Symposium: American Association of Petroleum Geologists Memoir 1, p. 108–121, https://doi.org/10.1306/M1357.

Embry, A.F., and Klovan, J.E., 1971, A Late Devonian reef tract on northeastern Banks Island, NWT: Bulletin of Canadian Petroleum Geology, v. 19, no. 4, p. 730–781, https://doi.org/10.35767/gscpgbull.19.4.730.

Fairhurst, B., Ewing, T., and Lindsay, B., 2021, West Texas (Permian) super basin, United States: Tectonics, structural development, sedimentation, petroleum systems, and hydrocarbon reserves: American Association of Petroleum Geologists Bulletin, v. 105, no. 6, p. 1099–1147, https://doi.org/10.1306/03042120130.

Ferrill, D.A., Cawood, A.J., Evans, M.A., Smart, K.J., King, R., and Zanoni, G., 2024, Thrust v. stylolite: Journal of Structural Geology, v. 182, https://doi.org/10.1016/j.jsg.2024.105113.

Fredrich, J.T., Evans, B., and Wong, T.F., 1990, Effect of grain size on brittle and semibrittle strength: Implications for micromechanical modelling of failure in compression: Journal of Geophysical Research: Solid Earth, v. 95, no. B7, p. 10,907–10,920, https://doi.org/10.1029/JB095iB07p10907.

Gray, J.M.N.T., 2018, Particle segregation in dense granular flows: Annual Review of Fluid Mechanics, v. 50, no. 1, p. 407–433, https://doi.org/10.1146/annurev-fluid-122316-045201.

Gray, J.M.N.T., and Ancey, C., 2011, Multi-component particle size segregation in shallow granular avalanches: Journal of Fluid Mechanics, v. 678, p. 535–588, https://doi.org/10.1017/jfm.2011.138.

Hill, C.A., 1996, Geology of the Delaware Basin: Guadalupe, Apache, and Glass Mountains, New Mexico and West Texas: Midland, Texas, Permian Basin Section, Society for Sedimentary Geology (SEPM) Publication 96-39, 480 p.

Hoblitt, R.P., 1986, Observations of the Eruptions of July 22 and August 7, 1980, at Mount St. Helens, Washington: U.S. Geological Survey Professional Paper 1335, 44 p., https://doi.org/10.3133/pp1335.

Hodgetts, D., Seers, T., Head, W., and Burnham, B.S., 2015, High performance visualisation of multiscale geological outcrop data in single software environment, *in* Mozetic, M., ed., Proceedings of the 77th EAGE Conference and Exhibition 2015: Earth Science for Energy and Environment: Madrid, Spain, European Association of Geoscientists & Engineers, p. 1100–1105, https://doi.org/10.3997/2214-4609.201412862.

Hornbuckle, J.S., III, 2017, Process Sedimentology of the Guadalupian Rader Limestone, Delaware Basin [M.S. thesis]: Norman, Oklahoma, USA, University of Oklahoma, 107 p.

Hunt, D.W., Fitchen, W.M., and Koša, E., 2003, Syndepositional deformation of the Permian Capitan reef carbonate platform, Guadalupe Mountains, New Mexico, USA: Sedimentary Geology, v. 154, no. 3–4, p. 89–126, https://doi.org/10.1016/S0037-0738(02)00104-5.

Iverson, R.M., 1997, The physics of debris flows: Reviews of Geophysics, v. 35, no. 3, p. 245–296, https://doi.org/10.1029/97RG00426.

Janson, X., Kerans, C., Loucks, R., Marhx, M.A., Reyes, C., and Murguia, F., 2011, Seismic architecture of a Lower Cretaceous platform-to-slope system, Santa Agueda and Poza Rica fields, Mexico: AAPG Bulletin, v. 95, no. 1, p. 105–146, https://doi.org/10.1306/06301009107.

Jobe, Z.R., Howes, N., Martin, J., Meyer, R., Coutts, D., Hou, P., and Laugier, F., 2021, Sedimentary graphic logs: A template for description and a toolkit for digitalization: The Sedimentary Record, v. 19, no. 3, p. 15–29, https://doi.org/10.2110/sedred.2021.3.3.

Johnson, C.G., Kokelaar, B.P., Iverson, R.M., Logan, M., LaHusen, R.G., and Gray, J.M.N.T., 2012, Grain-size segregation and levee formation in geophysical mass flows: Journal of Geophysical Research: Earth Surface, v. 117, https://doi.org/10.1029/2011JF002185.

Karakitsios, V., 2013, Western Greece and Ionian Sea petroleum systems: AAPG Bulletin, v. 97, no. 9, p. 1567–1595, https://doi.org/10.1306/02221312113.

Katz, D.A., Playton, T.E., Bellian, J.A., Harris, P.M., Harrison, C., and Maharaja, A., 2010, Slope heterogeneity and production results in a steep-sided Upper Paleozoic isolated carbonate platform reservoir, Karachaganak Field, Kazakhstan, *in* Proceedings of the Society of Petroleum Engineers (SPE) Caspian Carbonates Technology Conference, Atyrau, Kazakhstan, 8–10 November 2010: Denver, Colorado, USA, Society of Petroleum Engineers, SPE-139960-MS, https://doi.org/10.2118/139960-MS.

Kerans, C., 1985, Petrology of Devonian and Carboniferous Carbonates of the Canning and Bonaparte Basins: Perth, Australia, Western Australia Mining and Petro-

leum Research Institute Report 12, 203 p. (accessed April 2024).

Kerans, C., and Kempter, K., 2002, Hierarchical stratigraphic analysis of a carbonate platform, Permian of the Guadalupe Mountains: American Association of Petroleum Geologists Datapages Discovery Series 5 [CD-ROM].

Kerans, C., and Tinker, S.W., 1999, Extrinsic stratigraphic controls on development of the Capitan reef complex, *in* Saller, A.H., Harris, P.M., Kirkland, B.L., and Mazzullo, S.J., eds., Geologic Framework of the Capitan Reef: Society for Sedimentary Geology (SEPM) Special Publication 65, p. 15–36, https://doi.org/10.2110/pec.99.65.0015.

Kerans, C., Bellian, J.A., Playton, T.E., Harman, C., Rush, J., and Frost, E.L., III, 2012, 3-D sequence framework of Leonardian through Guadalupian shelf-to-basin successions of the Guadalupe Mountains, *in* Kerans, C., and Bellian, J.A., eds., Digital Geospatial Context for 3-D Source-to-Sink Models: New Insights into the Classic Shelf to Basin System of the Guadalupe and Delaware Mountains: SEPM Research Conference Extended Abstracts, 26–30 April 2012: Midland, Texas, USA, Society for Sedimentary Geology (SEPM), p. 45–57.

Kerans, C., Playton, T., Phelps, R., Scott, S.Z., Verwer, K., and Harris, P.M., 2014, Ramp to rimmed shelf transition in the Guadalupian (Permian) of the Guadalupe Mountains, *in* Verwer, K., Playton, T.E., and Harris, P.M., eds., Deposits, Architecture, and Controls of Carbonate Margin, Slope, and Basinal Settings: Society for Sedimentary Geology (SEPM) Special Publication 105, p. 26–49, https://doi.org/10.2110/sepmsp.105.13.

Kerans, C., Zahm, C., Garcia-Fresca, B., and Harris, P.M., 2021, Natural laboratory for studying stratigraphic architecture, facies tract distribution, and syndepositional deformation in carbonate ramps and steep-rimmed platforms: Guadalupe Mountains, west Texas and New Mexico, *in* Wright, V.P., and Della Porta, G., eds., Field Guides to Exceptionally Exposed Carbonate Outcrops: Gent, Belgium, International Association of Sedimentologists, p. 129–178, https://doi.org/10.54780/IASFG3/03.

King, P.B., 1948, Geology of the Southern Guadalupe Mountains, Texas: U.S. Geological Survey Professional Paper 215, 183 p., https://doi.org/10.3133/pp215.

Kokelaar, B.P., Graham, R.L., Gray, J.M.N.T., and Vallance, J.W., 2014, Fine-grained linings of leveed channels facilitate runout of granular flows: Earth and Planetary Science Letters, v. 385, p. 172–180, https://doi.org/10.1016/j.epsl.2013.10.043.

Koša, E., and Hunt, D.W., 2005, Growth of syndepositional faults in carbonate strata: Upper Permian Capitan platform, New Mexico, USA: Journal of Structural Geology, v. 27, no. 6, p. 1069–1094, https://doi.org/10.1016/j.jsg.2005.02.007.

Koša, E., and Hunt, D.W., 2006, Heterogeneity in fill and properties of karst-modified syndepositional faults and fractures: Upper Permian Capitan Platform, New Mexico, USA: Journal of Sedimentary Research, v. 76, no. 1, p. 131–151, https://doi.org/10.2110/jsr.2006.08.

Kvale, E.P., Bowie, C.M., Flenthrope, C., Mace, C., Parrish, J.M., Price, B., and DiMichele, W.A., 2020, Facies variability within a mixed carbonate-siliciclastic sea-floor fan (upper Wolfcamp Formation, Permian, Delaware Basin, New Mexico): AAPG Bulletin, v. 104, no. 3, p. 525–563, https://doi.org/10.1306/06121917225.

Laubach, S.E., Olson, J.E., and Gross, M.R., 2009, Mechanical and fracture stratigraphy: AAPG Bulletin, v. 93, no. 11, p. 1413–1426, https://doi.org/10.1306/07270909094.

Laubach, S.E., et al., 2019, The role of chemistry in fracture pattern development and opportunities to advance interpretations of geological materials: Reviews of Geophysics, v. 57, no. 3, p. 1065–1111, https://doi.org/10.1029/2019RG000671.

Lawson, E.C., 1989, Subaqueous Gravity Flows and Associated Deposits in the Rader Member, Capitan Reef Complex (Permian), Delaware Mountains, West Texas [M.S. thesis]: Madison, Wisconsin, USA, University of Wisconsin–Madison, 161 p.

Li, P., Kneller, B., and Valdez Buso, V., 2025, Carbonate-rich megabeds within a Triassic siliciclastic deep-water system, West Qinling orogenic belt, Central China: Character, processes and implications: The Depositional Record: A Journal of Biological, Physical and Geochemical Sedimentary Processes, v. 11, no. 1, p. 232–259, https://doi.org/10.1002/dep2.301.

Locat, P., Couture, R., Locat, J., Leroueil, S., and Jaboyedoff, M., 2006, Fragmentation energy in rock avalanches: Canadian Geotechnical Journal, v. 43, p. 830–851, https://doi.org/10.1139/t06-045.

Lokier, S.W., and Al Junaibi, M., 2016, The petrographic description of carbonate facies: Are we all speaking the same language?: Sedimentology, v. 63, no. 7, p. 1843–1885, https://doi.org/10.1111/sed.12293.

Machette, M.N., and Jochems, A.P., compilers, 2015, Fault number 2058, Guadalupe fault, *in* Quaternary Fault and Fold Database for the United States: Reston, Virginia, USA, U.S. Geological Survey, https://www.usgs.gov/natural-hazards/earthquake-hazards/faults (accessed December 2025).

Magnarini, G., Mitchell, T.M., Goren, L., Grindrod, P.M., and Browning, J., 2021, Implications of longitudinal ridges for the mechanics of ice-free long runout landslides: Earth and Planetary Science Letters, v. 574, https://doi.org/10.1016/j.epsl.2021.117177.

Marc, O., Turowski, J.M., and Meunier, P., 2021, Controls on the grain size distribution of landslides in Taiwan: The influence of drop height, scar depth and bedrock strength: Earth Surface Dynamics, v. 9, no. 4, p. 995–1011, https://doi.org/10.5194/esurf-9-995-2021.

Mazzuca, N., Bruni, A., and Joppen, T., 2015, Exploring the potential of deep targets in the South Adriatic Sea: Insight from 2D basin modeling of Croatian offshore: Geologia Croatica, v. 68, no. 3, p. 237–246, https://doi.org/10.4154/GC.2015.18.

McIlreath, I.A., and James, N.P., 1978, Carbonate slopes, *in* Walker, R.G., ed., Facies Models: St. John's, Newfoundland, Canada, Geological Association of Canada, Geoscience Canada Series, p. 245–257.

Middleton, G.V., 1970, Experimental studies related to problems of flysch sedimentation, *in* Lajoie, J., ed., Flysch Sedimentology in North America: Geological Association of Canada Special Paper 7, p. 253–272.

Moreland, T.W., 2018, Catastrophic Process Event Stratigraphy of the Rader Member in the Delaware Basin [M.S. thesis]: Norman, Oklahoma, USA, University of Oklahoma, 107 p.

Mullin, T., 2000, Coarsening of self-organised clusters in binary mixtures of particles: Physical Review Letters, v. 84, p. 4741–4744, https://doi.org/10.1103/PhysRevLett.84.4741.

Mullins, H.T., and Cook, H.E., 1986, Carbonate apron models: Alternatives to the submarine fan model for paleoenvironmental analysis and hydrocarbon exploration: Sedimentary Geology, v. 48, p. 37–79, https://doi.org/10.1016/0037-0738(86)90080-1.

Narr, W., Flodin, E.A., Playton, T.E., and Heesakkers, V., 2024, Depositional and lithological control on fractures in a steep, reefal carbonate margin: Lennard Shelf outcrops of the Canning Basin, Western Australia: AAPG Bulletin, v. 108, no. 8, p. 1443–1484, https://doi.org/10.1306/02132423039.

Nemec, W., 1990, Aspects of sediment movement on steep delta slopes, *in* Colella, A., and Prior, D.B., eds., Coarse-Grained Deltas: International Association of Sedimentologists Special Publication 10, p. 29–73, https://doi.org/10.1002/9781444303858.ch3.

Newell, N.D., Rigby, J.K., Fischer, A.G., Whiteman, A.J., Hickox, J.E., and Bradley, J.S., 1953, The Permian Reef Complex of the Guadalupe Mountains Region, Texas and New Mexico: A Study in Paleoecology: San Francisco, California, USA, W.H. Freeman and Company, 236 p.

Ortega, O.J., Gale, J.F.W., and Marrett, R., 2010, Quantifying diagenetic and stratigraphic controls on fracture intensity in platform carbonates: An example from the Sierra Madre Oriental, northeast Mexico: Journal of Structural Geology, v. 32, no. 12, p. 1943–1959, https://doi.org/10.1016/j.jsg.2010.07.004.

Perinotto, H., Schneider, J.-L., Bachèlery, P., Le Bourdonnec, F.-X., Famin, V., and Michon, L., 2015, The extreme mobility of debris avalanches: A new model of transport mechanism: Journal of Geophysical Research: Solid Earth, v. 120, no. 12, p. 8110–8119, https://doi.org/10.1002/2015JB011994.

Playton, T.E., 2008, Characterization, Variations, and Controls of Reef-Rimmed Carbonate Foreslopes [Ph.D. dissertation]: Austin, Texas, USA, University of Texas at Austin, 302 p.

Playton, T.E., and Kerans, C., 2018, Architecture and genesis of prograding deep boundstone margins and debris-dominated carbonate slopes: Examples from the Permian Capitan Formation, southern Guadalupe Mountains, west Texas: Sedimentary Geology, v. 370, p. 15–41, https://doi.org/10.1016/j.sedgeo.2017.12.021.

Playton, T.E., Janson, X., and Kerans, C., 2010, Carbonate slopes, *in* James, N.P., and Dalrymple, R.W., eds., Facies Models 4: St. John's, Newfoundland, Canada, Geological Association of Canada, p. 449–476.

Playton, T.E., Earnest, E., Fernández-Ibáñez, F., Bibolova, A., Tolessin, D., Tussupbayev, I., and Toleubay, B., 2025a, Fracture characterization from core and image log integration at Tengiz and Korolev fields, Kazakhstan: AAPG Bulletin, v. 109, no. 6, p. 807–843, https://doi.org/10.1306/04292523089.

Playton, T.E., Bellian, J.A., Kerans, C., and Katz, D., 2025b, Architecture and sequence stratigraphy of mixed carbonate-siliciclastic toe-of-slope systems: Examples from the Upper Permian Bell Canyon Members, Guadalupe Mountains, west Texas, *in* Proceedings, International Meeting for Applied Geoscience & Energy (IMAGE 2025), 25–28 August: Houston, Texas, USA, Society of Exploration Geophysicists.

Playton, T.E., Earnest, E., Fernández-Ibáñez, F., Bibolova, A., Tolessin, D., Tussupbayev, I., and Toleubay, B., 2025c, Insights on fracture and karst cavern origin and diagenesis from core observations at Tengiz and Korolev fields, Kazakhstan: AAPG Bulletin, v. 109, no. 6, p. 777–806, https://doi.org/10.1306/04292522159.

Ramsay, J.G., 1980, The crack-seal mechanism of rock deformation: Nature, v. 284, p. 135–139, https://doi.org/10.1038/284135a0.

Rigby, J.K., 1958, Mass movements in Permian rocks of Trans-Pecos Texas: Journal of Sedimentary Research, v. 28, no. 3, p. 298–315, https://doi.org/10.1306/74D707E0-2B21-11D7-8648000102C1865D.

Ruppel, S.C., ed., 2019, Anatomy of a Paleozoic Basin: The Permian Basin, USA: Bureau of Economic Geology Report of Investigations 285, 399 p., https://doi.org/10.23867/RI0285-1.

Rush, J., and Kerans, C., 2010, Stratigraphic response across a structurally dynamic shelf: The latest Guadalupian composite sequence at Walnut Canyon, New Mexico, USA: Journal of Sedimentary Research, v. 80, no. 9, p. 808–828, https://doi.org/10.2110/jsr.2010.073.

Sallenger, A.H., 1979, Inverse grading and hydraulic equivalence in grain-flow deposits: Journal of Sedimentary Research, v. 49, no. 2, p. 553–562, https://doi.org/10.1306/212F7789-2B24-11D7-8648000102C1865D.

Savage, S.B., and Lun, C.K.K., 1988, Particle size segregation in inclined chute flow of dry cohesionless granular solids: Journal of Fluid Mechanics, v. 189, p. 311–335, https://doi.org/10.1017/S002211208800103X.

Schultz, R.A., 2019, Geological Fracture Mechanics: Cambridge, UK, Cambridge University Press, 592 p., https://doi.org/10.1017/9781316996737.

Shackleton, J.R., Cooke, M.L., and Sussman, A.J., 2005, Evidence for temporally changing mechanical stratigraphy and effects on joint-network architecture: Geology, v. 33, p. 101–104, https://doi.org/10.1130/G20930.1.

Simabrata, H., Jobe, Z., Wood, L., Cardona, S., and Hou, P., 2025, Characterization, prediction and implications of compartments in a mixed carbonate-siliciclastic mass-transport complex: The Cutoff Formation, Permian Basin, Texas: Sedimentology, v. 72, no. 4, p. 1102–1131, https://doi.org/10.1111/sed.13269.

Spence, G.H., and Tucker, M.E., 1997, Genesis of limestone megabreccias and their significance in carbonate sequence stratigraphic models: A review: Sedimentary Geology, v. 112, p. 163–193, https://doi.org/10.1016/S0037-0738(97)00036-5.

Tanos, C.A., Oktaviani, A.D., Tiara, Y., Kusnandar, Y., and De Tulio, U., 2023, Ruby Field cores—The only proven carbonate debris-flow play in Indonesia, *in* Proceedings, Indonesian Petroleum Association Forty-Seventh Annual Convention & Exhibition, Indonesia, July 2023:

Jakarta, Indonesia, Indonesian Petroleum Association, paper IPA23-G-01.

Terzaghi, R.D., 1965, Sources of error in joint surveys: Geotechnique, v. 15, no. 3, p. 287–304, https://doi.org/10.1680/geot.1965.15.3.287.

Tinker, S.W., 1998, Shelf-to-basin facies distribution and sequence stratigraphy of a steep-rimmed carbonate margin: Capitan depositional system, McKittrick Canyon, New Mexico and Texas: Journal of Sedimentary Research, v. 68, p. 1146–1174, https://doi.org/10.2110/jsr.68.1146.

Vallance, J.W., and Savage, S.B., 2000, Particle segregation in granular flows down chutes, *in* Rosato, A.D., and Blackmore, D.L., eds., IUTAM Symposium on Segregation in Granular Flows: Dordrecht, Netherlands, Springer, Solid Mechanics and Its Applications, v. 81, p. 31–51, https://doi.org/10.1007/978-94-015-9498-1_3.

Wallace, M.W., Kerans, C., Playford, P.E., and McManus, A., 1991, Burial diagenesis in the Upper Devonian reef complexes of the Geikie Gorge region, Canning Basin, Western Australia: American Association of Petroleum Geologists Bulletin, v. 75, no. 6, p. 1018–1038, https://doi.org/10.1306/0C9B28B7-1710-11D7-8645000102C1865D.

Weidinger, J.T., Korup, O., Munack, H., Altenberger, U., Dunning, S.A., Tippelt, G., and Lottermoser, W., 2014, Giant rockslides from the inside: Earth and Planetary Science Letters, v. 389, p. 62–73, https://doi.org/10.1016/j.epsl.2013.12.017.

Wennberg, O.P., Azizzadeh, M., Aqrawi, A.M., Blanc, E., Brockbank, P., Lyslo, K.B., Pickard, N., Salem, L.D., and Svånå, T., 2007, The Khaviz anticline—An outcrop analogue to giant fractured Asmari Formation reservoirs in SW Iran, *in* Jolly, R.J.H., Rawnsley, K., and Sanderson, D.J., eds., Fractured Reservoirs: Geological Society, London, Special Publication 270, p. 23–42, https://doi.org/10.1144/GSL.SP.2007.270.01.02.

Wentworth, C.K., 1922, A scale of grade and class terms for clastic sediments: The Journal of Geology, v. 30, p. 377–392, https://doi.org/10.1086/622910.

Yang, K., and Dorobek, S.L., 1995, The Permian Basin of west Texas and New Mexico: Tectonic history of a "composite" foreland basin and its effects on stratigraphic development, *in* Dorobek, S.L., and Ross, G.M., eds., Stratigraphic Evolution of Foreland Basins: Society for Sedimentary Geology (SEPM) Special Publication 52, p. 149–174, https://doi.org/10.2110/pec.95.52.0149.

Yang, S., Wang, X., Liu, Q., and Pan, M., 2020, Numerical simulation of fast granular flow facing obstacles on steep terrains: Journal of Fluids and Structures, v. 99, https://doi.org/10.1016/j.jfluidstructs.2020.103162.

Zhang, S.L., Yin, Y.P., Hu, X.W., Wang, W.P., and He, X.R., 2023, Block–grain phase transition in rock avalanches: Insights from large-scale experiments: Journal of Geophysical Research: Earth Surface, v. 128, no. 11, https://doi.org/10.1029/2023JF007204.

Zhang, Y., Wong, L.N.Y., and Chan, K.K., 2019, An extended grain-based model accounting for microstructures in rock deformation: Journal of Geophysical Research: Solid Earth, v. 124, no. 1, p. 125–148, https://doi.org/10.1029/2018JB016165.

Science Editor: Troy Rasbury
Associate Editor: Youwei Wang

Manuscript Received 17 February 2026
Revised Manuscript Received 25 May 2026
Manuscript Accepted 1 October 2026